Mineralogical Magazine (2022), **86**, 459–477
doi:10.1180/mgm.2022.42

CAMBRIDGE UNIVERSITY PRESS

Article

Tracking mineral evolution and element mobility during albitisation and subsequent kaolinisation of phyllite rocks: A case study from the Verrucano of Monti Pisani, Tuscany, Italy

Massimo D'Orazio[1]*, Paolo Fulignati[1], Anna Gioncada[1] and Francesco Cavalcante[2]

[1]Dipartimento di Scienze della Terra, Università di Pisa, 56126 Pisa, Italy; and [2]Istituto di Metodologie per l'Analisi Ambientale–CNR, 85050 Tito Scalo, Italy

Abstract

This work describes the first occurrence of albitite rocks in the Middle Triassic Verruca Formation, Monti Pisani, Northern Apennines, northern Tuscany, Italy. The albitite formed by Na-metasomatism of phyllites ('potassic white mica' + quartz + 'chlorite' + hematite + albite) in an amagmatic environment. The albitisation process took place after the Miocene main phases of Apenninic deformation and was followed by the formation of veins of Fe-carbonate + quartz. Hydrothermal alteration progressed with the ingression, possibly favoured by the increase of permeability due to albitisation, of a slightly acidic, oxidising, aqueous fluid that led to the pervasive kaolinisation of the albitite and to the complete transformation of the Fe-carbonate of the veins into Fe-hydroxides. This stage was followed by supergene alteration that led to the formation of a pervasive network of halloysite veinlets and colloform (P–Al–Si)-bearing Fe-hydroxides. Finally, the hydrothermally altered rock underwent a localised brittle fracturing without new minerals being formed. The prominent compositional changes occurring during this multi-stage hydrothermal process were the inversion of the Na_2O/K_2O ratio of the whole rock (from 0.07 in the pristine phyllite to up to 200 for the kaolinised albitite), the loss of Fe and Mg, and the enrichment of Sb. The MREE were partially lost, whereas LREE and HREE behaved conservatively. Though pervasive hydrothermal alteration occurrences are common in central-southern Tuscany, mostly related to the post-collisional extensional regime, lithospheric thinning and emplacement of magmatic bodies in the crust, the rare Monti Pisani kaolinised albitite described in this investigation expands the effects of post-collisional hydrothermal activity in Tuscany northwards, far from potential magmatic sources.

Keywords: albitisation, hydrothermal alteration, kaolinisation, Monti Pisani, Northern Apennines, Verrucano

(Received 17 January 2022; accepted 15 April 2022; Accepted Manuscript published online: 13 May 2022; Associate Editor: Giancarlo Della Ventura)

Introduction

Albitisation is a metasomatic process activated by Na-rich fluids that, while infiltrating granitoid and metasedimentary rocks, leads to the transformation of feldspars of variable composition into albite and to the dissolution of quartz (Boulvais *et al.*, 2007; Engvik *et al.*, 2008; Petersson *et al.*, 2012; Condit *et al.*, 2018). Although commonly related to the late magmatic and subsolidus hydrothermal phases of the intrusion-related environment (e.g. Cathelineau, 1986, 1987; Charoy and Pollard, 1989; Kaur *et al.*, 2019; Pérez-Soba and Villaseca, 2019), the metasomatic process of albitisation has been recognised in a variety of geological contexts over a range of crustal conditions, from sedimentary-diagenetic (pseudomorphic replacement of detrital plagioclase by albite, Perez and Boles, 2005) to the amphibolite and even granulite metamorphic facies (Rubenach and Lewthwaite, 2002; Holness, 2003; Touret and Nijland, 2013). Albitisation is also a characteristic alteration facies of porphyry-style, iron oxide copper–gold ore deposits (IOCG) and uranium ore deposits (Pirajno, 2009 and references therein), and on a large scale can result in feldspathic deposits of economic importance (Castorina *et al.*, 2006).

In general, the albitisation processes active in a range of different environments can be related to two types of metasomatising fluids and circulation models: (1) dilute aqueous fluids circulating around cooling granite plutons, with salinity acquired by mixing with magmatic fluids or through water–rock interaction (e.g. Carten, 1986; Pirajno, 2009); and (2) high salinity chlorine and Na-rich fluids (Na is easily complexed by chlorine), being either surface-derived brines, infiltrating through faults in extensional settings, or subsurface waters acquiring high salinity by interaction with evaporite beds (Barton and Johnson, 1996; van de Kamp and Leake, 1996; Quesnel *et al.*, 2019; Cathelineau *et al.*, 2021). Aqueous fluids circulating along increasing temperature paths result in albitisation of feldspars together with quartz dissolution induced by temperature rise and consequent increase of quartz solubility.

Regardless of the origin of the Na-rich fluids, albitisation develops through a dissolution–precipitation mechanism, leading to an increase in porosity (Engvik *et al.*, 2008). An important consequence is the development of a transient (or permanent) permeability which enhances the infiltration of albitising fluids and the development of metasomatism (Boulvais *et al.*, 2007). Note

*Author for correspondence: Massimo D'Orazio, Email: massimo.dorazio@unipi.it
Cite this article: D'Orazio M., Fulignati P., Gioncada A. and Cavalcante F. (2022) Tracking mineral evolution and element mobility during albitisation and subsequent kaolinisation of phyllite rocks: A case study from the Verrucano of Monti Pisani, Tuscany, Italy. *Mineralogical Magazine* **86**, 459–477. https://doi.org/10.1180/mgm.2022.42

however, if permeability promotes albitisation on a large scale, it may leave the albitite prone to infiltration by later circulating fluids.

In most cases, albitisation has been recognised in granitic environments, although some papers have recognised that granite albitisation can also develop long after the hydrothermal activity associated with cooling of the intrusion, in which case the granitoid rocks only have a passive role (e.g. Engvik *et al.*, 2008; Kontonikas-Charos *et al.*, 2014). Notwithstanding the vast amounts of literature on albitisation, few papers report examples outside of the magmatic environment (e.g. van de Kamp and Leake, 1996). Moreover, the effects of the superposition of later fluid circulation has not been investigated, regardless of the increase of permeability during this metasomatic process.

In this paper, we present petrographic and geochemical data to describe fully an example of albitisation of Middle Triassic phyllites from Monti Pisani, northern Tuscany, Italy, and track the mineralogical and geochemical changes undergone by these rocks through a multi-stage (albitisation to kaolinisation) hydrothermal process. The latter occurred after the main Apenninic deformative phase, and is not related directly to any known magmatic-related hydrothermal activity. This aspect contrasts with other areas of southern Tuscany where hydrothermal activity is related to thermal anomalies induced by lithospheric thinning, generally coupled with post-collisional magmatism of Late Miocene to Quaternary age (e.g. Batini *et al.*, 2003).

Geological background

The Monti Pisani are a small mountainous massif belonging to the Northern Apennines, located in northern Tuscany, between the Arno and Serchio rivers (Fig. 1). They are part of the 'Middle Tuscan Ridge', a discontinuous belt of mountains and hills, from the Alpi Apuane massif to the north, to the Monte Argentario to the south, where the metamorphic units of the Northern Apennines are well exposed.

From east to west and from bottom to top the Monti Pisani are constituted by the Monte Serra Unit, the Santa Maria del Giudice Unit and the Tuscan Nappe (Fig. 1; Rau and Tongiorgi, 1974). The rocks cropping out in the study area belong to the Monte Serra Unit, which is made mainly of meta-siliciclastic rocks belonging to the Anisic-Ladinic Verruca and the Carnic Quarziti di Monte Serra formations. The protoliths of these rocks were continental siliciclastic sediments that initiated the Alpine sedimentary succession of the Northern Apennines. These rocks rest unconformably on a Palaeozoic basement (Cambrian?–Permian) composed of schist, phyllite, quartzite and meta-conglomerate (Rau and Tongiorgi, 1974; Paoli *et al.*, 2017). During the Alpine Orogeny these rocks underwent a polyphase tectono-metamorphic evolution, characterised by three main deformative events (D_1, D_2 and D_3; Leoni *et al.*, 2009). The first, and most intense, tectonic phase (D_1) produced tight to isoclinal F_1 folds associated with a penetrative S_1 axial plane foliation (slaty cleavage foliation). The F_1 folds have steep axial planes and vergences both towards the NE and SW. During this phase the rocks suffered a dynamic recrystallisation and were metamorphosed under greenschist-facies conditions (Franceschelli *et al.*, 1986; Leoni *et al.*, 2009). The most common mineral assemblage of the meta-siliciclastic rocks from Monti Pisani is quartz+muscovite ± 'chlorite' ± paragonite ± pyrophyllite ± albite with accessory amounts of 'tourmaline', hematite, magnetite, rutile, zircon, 'apatite', 'monazite', 'xenotime' and Fe-hydroxide replacing Fe-carbonate (e.g. Franceschelli *et al.*, 1987). The *P*–*T* conditions of this metamorphism are poorly constrained; however, most pressure and temperature estimates are in the range 0.4–0.7 GPa and 350–400°C, respectively (Franceschelli *et al.*, 1986; Franceschelli *et al.*, 1989; Franceschelli *et al.*, 1991; Leoni *et al.*, 2009). The tectonic phases that followed, D_2 and D_3, were much less intense than the former and typically did not produce significant metamorphic recrystallisation (Leoni *et al.*, 2009).

Field occurrence

The kaolinised albitite rocks described in this investigation are located in a wooded area in the central part of the Monti Pisani, ~650 m SE of Monte Zano (Vorno hamlet, Lucca) at an altitude of ~ 380 m a.s.l. and have not been described to date (Fig. 2). They crop out over a length of ~20 m and a height of ~1–2 m thanks to a road cut at 43°46'43"N, 10°31'37"E, whereas the surrounding area is characterised by a thick cover of soil and detritus (Fig. 3). The whitish to greyish earthy rocks are interposed between quartzite (east side) and phyllite (west side) belonging to the Anageniti minute Member of the Verruca Formation (Fig. 3) and are pervaded by a network of brown veins and veinlets of Fe-hydroxide (Fig. 4).

The transition from the kaolinised albitite to the country rocks is relatively abrupt towards the quartzite and more gradual towards the phyllite. Towards its western margin, the kaolinised albitite includes ragged masses of lead-grey to violet phyllite and fades gradually to the phyllite (Fig. 4a,b,d). The field observations, confirmed by thin section analysis, indicates that the kaolinised albitite formed at the expense of a phyllite protolith. The Fe-hydroxide veins are from a few mm up to 3 cm in width and can be followed for up to 1–2 m. They are very irregularly distributed, however two more frequent sets of veins can be recognised that are subvertical and strike N110 and N60 (Fig. 4b,c). When crushing this material, many grains with an obvious rhombohedral habit are observed. Very probably, the veins were originally Fe-bearing carbonates (possibly siderite) replaced successively by Fe-hydroxide. Where the veins crosscut the phyllite, they typically exhibit a white halo (Fig. 4b). Quartz veins, up to 2 cm in width, also occur. They are locally deformed and generally follow the main pervasive foliation of the country rocks which is sub-parallel to bedding, trends N23 and dips 82W; cross-cutting relationships reveal that the quartz veins predate the Fe-hydroxide ones. Finally, a network of tiny veinlets (up to 2 mm in width) of whitish material pervades the kaolinised albitite (Fig. 4e). Rarely, we observed the occurrence of breccia structures within the kaolinised albitite (Fig. 4f).

Samples and analytical methods

Ten samples considered representative of all the types of rocks in the outcrop were selected for the petrographic, mineralogical and geochemical study.

Mineralogical and textural features of the samples were examined in polished thin sections with optical (Zeiss Axioplan) and electron (Philips XL30 and FEI Quanta 450 ESEM FEG) microscopy. Polished thin sections were carbon-coated before electron microscopy. X-ray maps (800 × 532 grid, 30 min acquisition time) were obtained with a FEI Quanta 450 ESEM FEG using the *Kα* radiation of the elements Na, Mg, Al, Si, K, Ti and Fe. Scanning electron microscopy (SEM) analyses were performed at the Pisa University's Dipartimento di Scienze della Terra

https://doi.org/10.1180/mgm.2022.42 Published online by Cambridge University Press

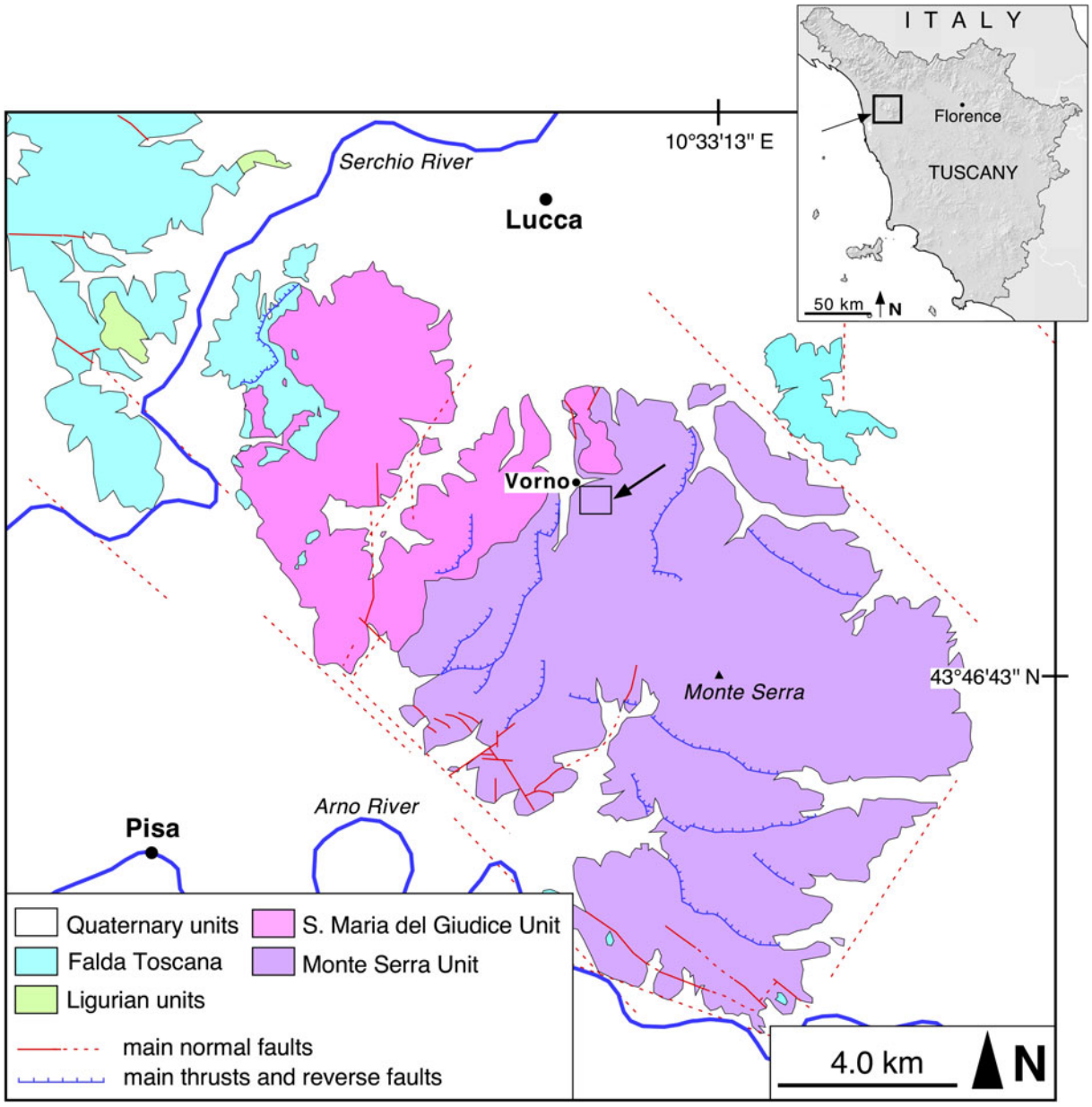

Fig. 1. Tectonic sketch map of the Monti Pisani area (Lucca and Pisa provinces, Tuscany). The small square encloses the area represented in Fig. 2. Redrawn and simplified from Rau and Tongiorgi (1974).

(hereafter DST-UniPi; Philips XL30) and at Centro per l'Integrazione della Strumentazione Scientifica dell'Università di Pisa (CISUP; FEI Quanta 450 ESEM FEG).

A tiny vein of white material taken from a kaolinised albitite sample was dispersed in water and left to settle. Then a few drops of the supernatant were deposited on a thin-section glass slide and evaporated. This preparation was carbon-coated and examined with the FEI Quanta 450 ESEM FEG at very high magnification (up to × 260,000).

Powder X-ray diffraction (PXRD) was performed for the identification and quantification of mineral phases using a Rigaku DMax 2200 diffractometer equipped with Cu*K*α radiation, a scintillation counter detector and sample spinner (Istituto di Metodologie per l'Analisi Ambientale (IMAA-CNR), Tito Scalo). Data were collected between 2–70°2θ and 2–32°2θ angles for the bulk sample and clay fraction, respectively, with a 0.02°2θ step size and 3 s for each step, power = 40 kV and current = 30 mA. The clay fraction was separated by settling in distilled water. Oriented mounts were prepared by settling a suspension after being saturated with Mg^{2+} cations using 1 N $MgCl_2$ solution, and each specimen was air dried, glycolated at 60°C for 8 hours and heated at 375°C for 1 hour (Moore and Reynolds, 1997). Quantitative analyses were carried out on bulk sample XRD profiles by measuring the peak area of both phyllosilicates and non-phyllosilicates (Cavalcante *et al.*, 2007) using the *Winfit* computer program (Krumm, 1999). The results obtained by PXRD were calibrated with whole-rock major-element data obtained by inductively coupled plasma optical emission spectrometry (ICP-OES) and LOI values, using the experimental software *vbAffina* (Leoni *et al.*, 2008; Cesarano *et al.*, 2018).

https://doi.org/10.1180/mgm.2022.42 Published online by Cambridge University Press

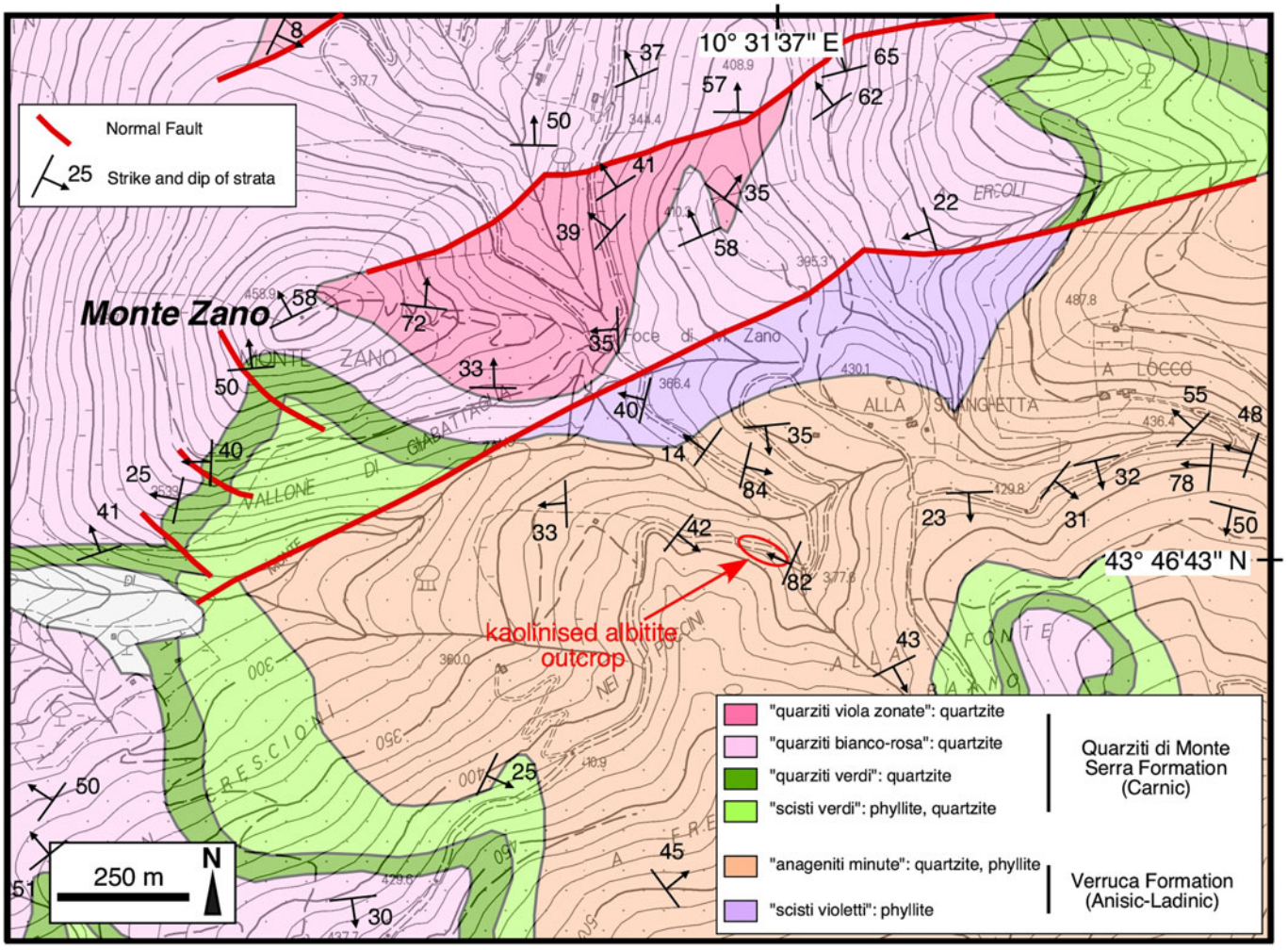

Fig. 2. Geological map of the Monte Zano area (Monti Pisani, Lucca province). The red ellipse encloses the study area. Redrawn and simplified from Rau and Tongiorgi (1974), and integrated with measurements from this work.

The major-element concentrations of the bulk-rock samples were determined by ICP-OES following lithium metaborate/tetraborate fusion and dilute HNO_3 dissolution (detection limits = 0.01 wt.% or better) at Actlabs (Ancaster, Ontario, Canada).

The concentrations of 37 trace elements in the whole-rock samples were determined by inductively coupled plasma mass spectrometry (ICP-MS, Perkin-Elmer NexION 300x at DST-UniPi.) following HF + HNO_3 dissolution at low and high pressure. At the element concentrations in the samples investigated precision is better than 5% RSD, except for Sc, Cu, Zn and Pb in which the precision is between 5 and 10% RSD. Mercury has been determined by atomic absorption spectrometry

Fig. 3. The outcrop of the kaolinised albitite rock investigated in this study. The locations of some of the samples are also reported. See also Fig. 4.

https://doi.org/10.1180/mgm.2022.42 Published online by Cambridge University Press

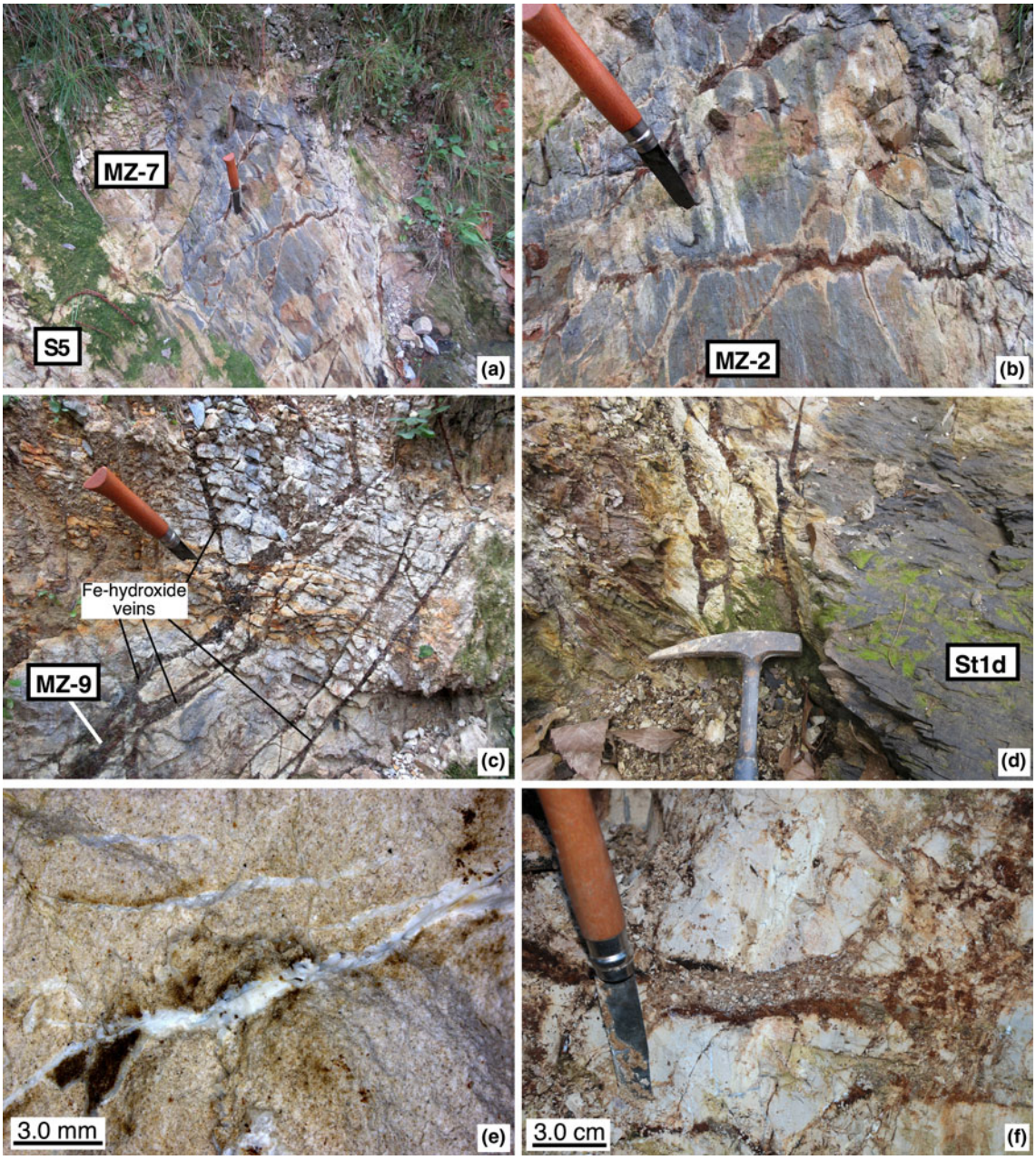

Fig. 4. Details of the kaolinised albitite outcrop: (a) westernmost part of the outcrop showing ragged relicts of the lead-grey phyllite protolith; (b) detail of the same outcrop as (a) showing several Fe-hydroxide veins with white halos; (c) Fe-hydroxide veins cross-cutting the whitish kaolinised albitite; (d) detailed view of the transitional contact (western side) between the hydrothermally altered rock (left) and the unaffected phyllite protolith (right); (e) veinlets of halloysite cross-cutting the kaolinised albitite; (f) detail of the breccia structure within the kaolinised albitite. The locations of some of the samples are also shown. See also Fig. 3.

(AAS) using a Milestone direct mercury analyser (DMA 80 Tri Cell; detection limit ≈ 0.5 ng/g for a sample weight of 100 mg).

A fluid-inclusion investigation was carried out on quartz crystals separated from the breccia, shown in Fig. 4f. Doubly polished quartz crystals (thickness 100–300 μm) were prepared for petrography and microthermometric determinations. The thermometric behaviour of fluid inclusions was studied on a Linkam THMS 600 heating-freezing stage (DST-UniPi), and the accuracy of measurements is estimated at ± 2°C at 398°C, controlled by the melting point of $K_2Cr_2O_7$, ± 0.1°C at 0°C and ± 0.2°C at −56.6°C, controlled by using certified pure water and CO_2-bearing synthetic fluid inclusions.

Results

Petrography and mineralogy

The protolith

Three samples of the protolith of the kaolinised albitite rock described in this study were collected. One (sample MZ-1) was taken west of the kaolinised albitite outcrop just out of the alteration zone, whereas the other two (St1d and MZ-2) were taken within the kaolinised albitite outcrop, in the least altered portions (Fig. 4a,b). Sample MZ-1 is a lead-grey to violet-grey phyllite that, together with quartzite, meta-sandstone and meta-conglomerate, forms the Anageniti minute member of the Verruca Formation

https://doi.org/10.1180/mgm.2022.42 Published online by Cambridge University Press

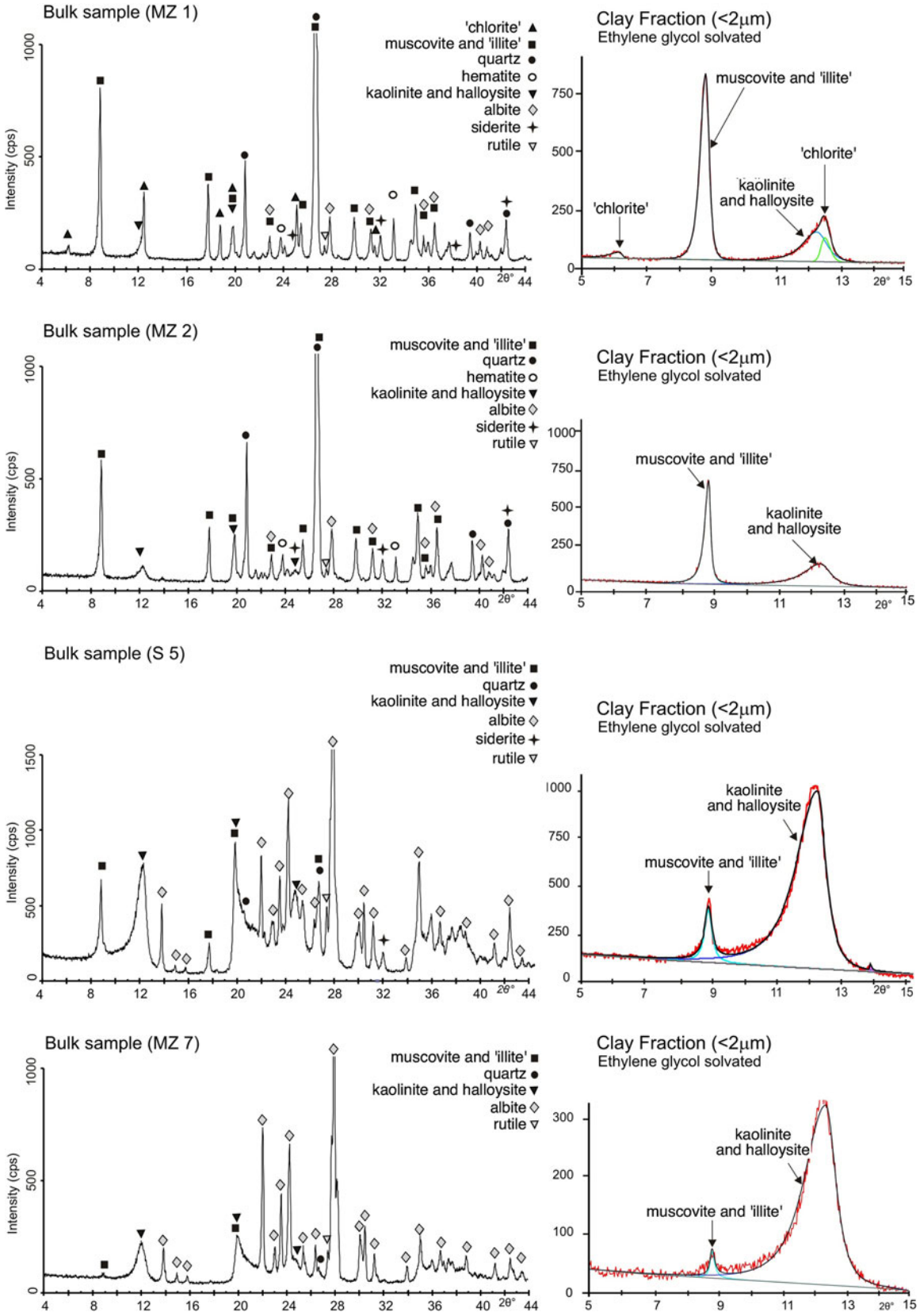

Fig. 5. Powder X-ray diffraction patterns. The diagrams to the right show the X-ray diffraction of the clay fraction of the samples solvated with ethylene glycol.

https://doi.org/10.1180/mgm.2022.42 Published online by Cambridge University Press

Table 1. Mineralogical composition (wt.%) of the bulk samples determined by PXRD.

Sample	Rock type	Qz	Ab	Sd	Hem	Rt	Ms/ Ilt	Chl	Kln/ Hly
MZ-1	phyllite protolith	26.0	2.0	2.5	3.5	1.0	54.0	7.0	4.0
MZ-2	phyllite protolith	36.0	4.0	2.0	3.0	1.0	50.0	n.d.	4.0
S5	partially altered protolith	3.0	22.0	1.0	n.d.	1.0	20.0	n.d.	53.0
MZ-7	kaolinised albitite	tr	52.0	1.0	tr	1.5	1.0	n.d.	44.5

Qz, quartz; Ab, albite; Sd, siderite; Hem, hematite; Rt, rutile; Ms, muscovite; Ilt, 'illite'; Chl, 'chlorite'; Kln, kaolinite; Hly, halloysite; tr, trace; n.d., not detected.

(Franceschelli *et al.*, 1987). Petrographically, this fine-grained rock has a well-developed schistosity and is composed predominantly of 'potassic white mica' (muscovite and/or 'illite') + quartz with minor amounts of 'chlorite' + hematite + albite. Accessory phases are 'tourmaline', zircon, xenotime-(Y), monazite-(Ce), 'apatite', rutile and Fe-carbonates. Samples St1d and MZ-2 are similar to sample MZ-1, except for their much lower content of hematite and 'chlorite', and their slightly higher content of quartz and albite. The proportion of hematite and 'chlorite' in the protolith rocks correlates with their hand-specimen colour that changes from lead-grey/violet-grey to pearly white as the amounts of these ferromagnesian minerals decrease. Samples MZ-1 and MZ-2 were investigated by PXRD, which shows that sample MZ-2 does not contain 'chlorite', carries a small amount of kaolinite/halloysite; and is characterised by a lower 'potassic white mica'/quartz ratio with respect to sample MZ-1 (Fig. 5; Table 1).

The X-ray maps of samples MZ-1 and MZ-2 (Fig. 6) show the high abundance of quartz and 'potassic white mica' of these rocks, and the slight increase and decrease of albite and ferromagnesian minerals, respectively, from MZ-1 to MZ-2. A sample of quartzite (S4) has been collected from the easternmost border of the

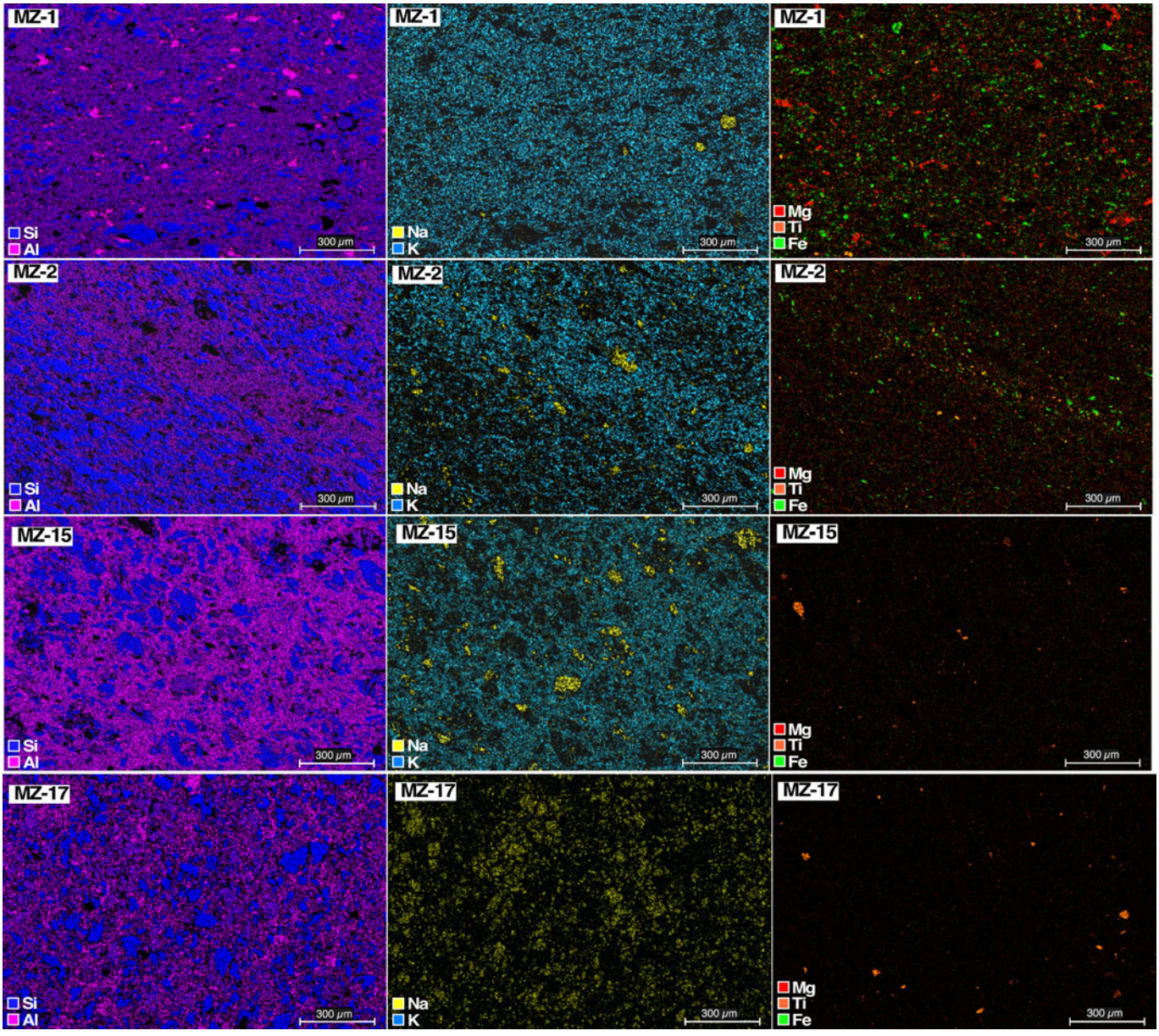

Fig. 6. X-ray maps (*Kα* radiation of Si, Al, Na, K, Mg, Fe and Ti).

https://doi.org/10.1180/mgm.2022.42 Published online by Cambridge University Press

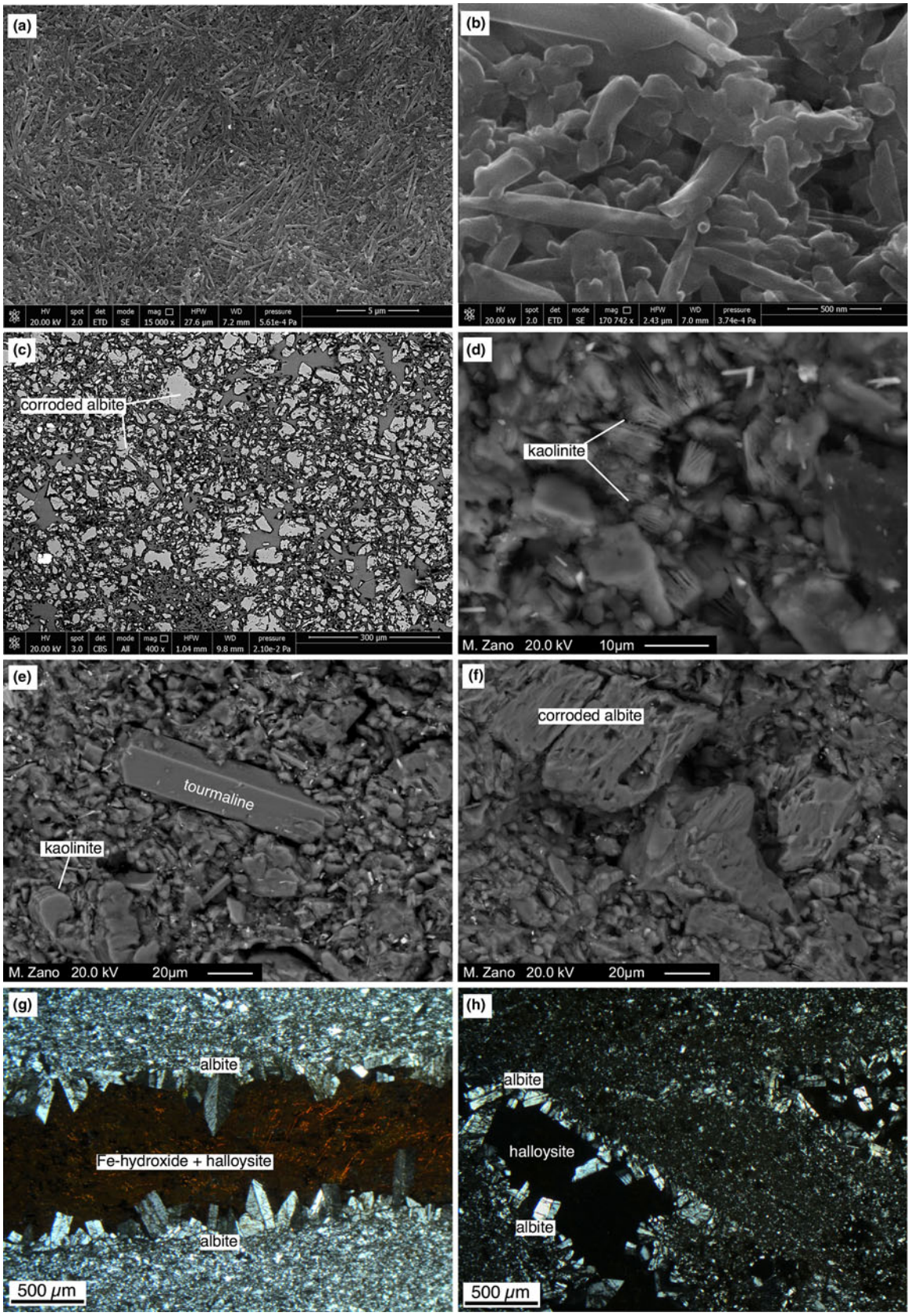

Fig. 7. Images of the kaolinised albitite: (a) FEG-SEM SE image nanotubes of halloysite; (b) FEG-SEM SE image nanotubes of halloysite taken at high magnification (×170,000); (c) FEG-SEM back-scatter electron (BSE) image at low magnification showing corroded albite crystals (light grey) with kaolinite + halloysite (dark grey); (d) SEM BSE image of flaky kaolinite crystals; (e) SEM BSE image of a euhedral, residual 'tourmaline' crystal within a matrix of kaolinite + albite; (f) SEM BSE image of a strongly corroded larger albite crystal within a matrix of kaolinite + albite; (g,h) optical microscope images (crossed polars) of a micro-vein (g) and micro-vugs (h) lined by euhedral albite crystals and filled by Fe-hydroxide + halloysite and halloysite, respectively.

https://doi.org/10.1180/mgm.2022.42 Published online by Cambridge University Press

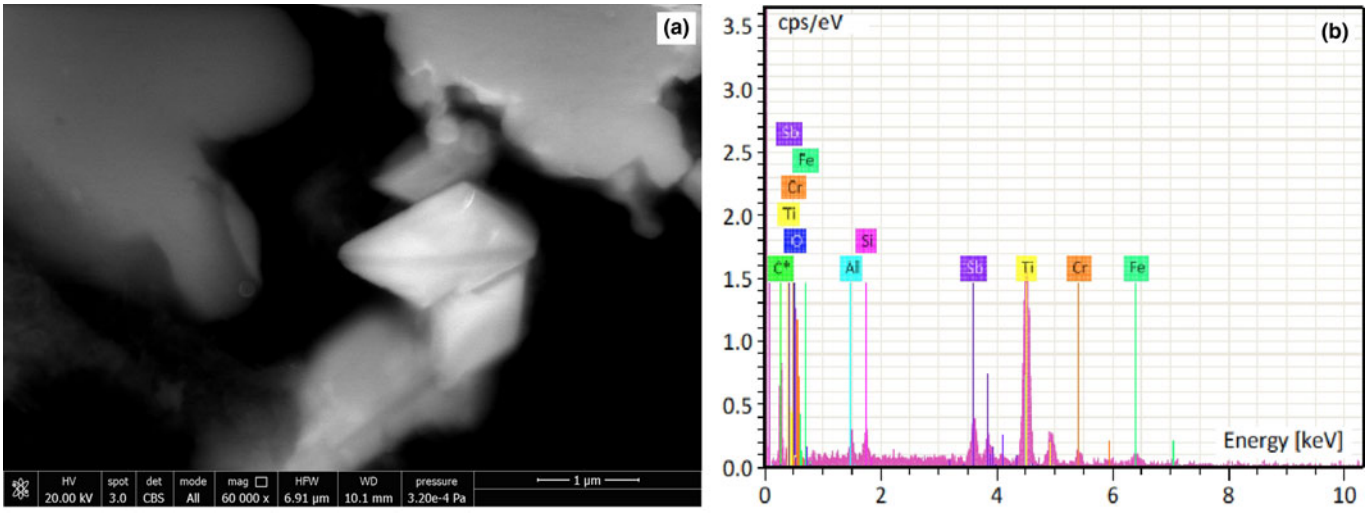

Fig. 8. (a) FEG-SEM BSE image of a tiny euhedral crystal of the Sb(Cr,Fe,Si,Al)-bearing Ti oxide phase in sample MZ-7; (b) SEM-EDX spectrum of the crystal.

outcrop. This rock is dominated by quartz with less abundant 'potassic white mica' and minor amounts of 'chlorite' and albite. The accessory minerals observed are the same as those found in the phyllites. Samples S5 and MZ-15 have petrographic features intermediate between those of the phyllite protolith and kaolinised albitite. Indeed, X-ray maps (Fig. 6; MZ-15 sample) and PXRD data (Fig. 5; sample S5) provide evidence that these rocks are characterised by slightly lower abundances of 'potassic white mica' and ferromagnesian minerals and by a higher content of albite with respect to the phyllite protolith.

The kaolinised albitite

The kaolinised albitite (samples MZ-7, MZ-17 and S6) is whitish or light orange in colour. It is earthy and friable, crossed by irregular dark brown veins and veinlets of Fe-hydroxides (1 mm to 3–4 cm in width), and pervaded by a network of tiny veins (~0.1 mm to ~2 mm in width) of pearly-white and compact material mostly comprising halloysite (Figs 4e, 7a,b).

Optical and scanning electron microscopy shows that these samples consist of variable amounts of albite + kaolinite (± halloysite) + quartz ± 'potassic white mica' (Fig. 7c,d,f). Accessory minerals are rutile, monazite-(Ce), zircon, xenotime-(Y) and 'tourmaline' (Fig. 7e). We also found tiny (~1 µm) euhedral crystals and larger rounded grains of a Sb(Cr,Fe,Si,Al)-bearing Ti oxide (Fig. 8) with up to ~13 wt.% Sb (SEM-EDX semi-quantitative analyses). The major minerals (albite + kaolinite and halloysite) of these rocks (sample MZ-7) were also identified by PXRD (Fig. 5).

The X-ray maps of sample MZ-17 (Fig. 6) show the abundance of quartz, kaolinite (± halloysite) and albite and the complete lack of K-bearing minerals.

Most of the albite crystals appear extensively corroded (Fig. 7c,f). Within the same samples we observed veinlets and micro-vugs, a few mm in size, lined with coarser euhedral (sometimes having rounded edges) albite crystals (up to 5–600 µm in length; Fig. 7g,h). The latter protrude into homogeneous masses of halloysite and Fe-hydroxides pseudomorphing Fe-carbonate (Figs 7g,h, 9a–d). Iron hydroxide also replaces euhedral Fe-carbonate crystals within the matrix of the kaolinised albitite (Fig. 9e,f). These pseudomorphs enclose tiny euhedral quartz crystals and strongly corroded albite. The same mineral association, though with a higher proportion of Fe-hydroxides replacing Fe-carbonates, also characterises the larger veins cross-cutting the kaolinised albitite. The rare brecciated rocks within the kaolinised albitite (Fig. 4f) are composed of small clasts (~80% by volume), from 0.5 to 8 mm in size, dominated by kaolinised albitite and Fe-hydroxide vein fragments with less abundant euhedral quartz and albite crystal fragments. The fine-grained matrix (<300 µm) is made of the same minerals. No evidence of newly-formed cementing minerals have been found.

Geochemistry

The protolith

The major-element composition of the phyllite protolith falls within the typical range of phyllites of the Verruca Formation from Monti Pisani (Franceschelli *et al.*, 1987). These rocks are characterised by low Na_2O/K_2O ratios (0.07–0.14; Fig. 10) in agreement with the low and high abundance of albite and 'potassic white mica', respectively (Table 2). The concentrations of TiO_2, total Fe_2O_3 and MgO are in keeping with the abundance of hematite, 'chlorite' and rutile. The intermediate samples S5 and MZ-15 have Na_2O and K_2O contents intermediate between those of the kaolinised albitite and the unaltered phyllite, though closer to the latter.

The trace-element distributions of the phyllite protolith are comparable to that of the average Upper Continental Crust (Taylor and McLennan, 1995) and the average Phanerozoic Shale (Condie, 1993; Fig. 11a; Table 3). The most notable exceptions are the concentration of Sr, which is much lower, and those of Sb and Cs, which are higher. The low Sr content is a typical feature of the meta-siliciclastic rocks of the Monte Serra Unit, which are characterised by very low, and low, abundances of Ca–Mg carbonates and feldspars, respectively (Franceschelli *et al.*, 1987). The positive anomaly of Sb seems to be a peculiar feature of the meta-sedimentary rocks investigated. The high content of Cs is in agreement with the abundance of 'potassic white mica' and correlates with the high K_2O content (4.37–5.55 wt.%)

https://doi.org/10.1180/mgm.2022.42 Published online by Cambridge University Press

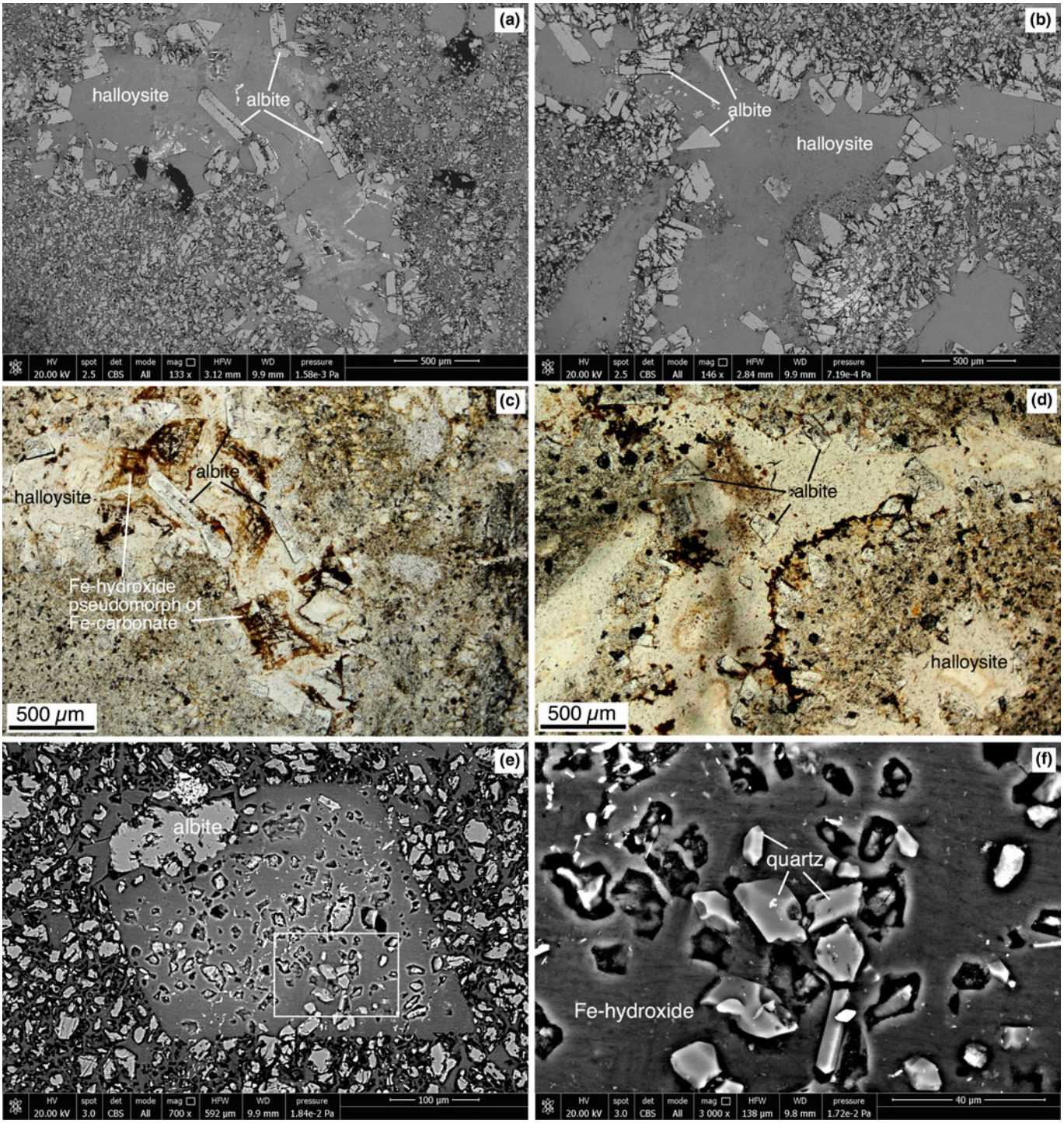

Fig. 9. Petrography of the kaolinised albitite: (a,b) FEG-SEM BSE images showing micro-vugs lined with coarse euhedral albite crystals and filled with homogeneous masses of kaolinite/halloysite and Fe-hydroxide; (c,d) optical microscope images (plane polarised light) of the same area portrayed in (a) and (b) emphasising the occurrence of Fe-hydroxide (brown and black in colour) inside the micro-vugs; (e) FEG-SEM BSE images of the Fe-hydroxide replacing a euhedral rhombohedral crystal of Fe-carbonate enclosing many euhedral quartz crystals and strongly corroded albite; (f) enlarged view of the area enclosed in the white rectangle in (e) showing the tiny euhedral quartz crystals.

of the rocks studied (Upper Continental Crust = 3.37 wt.%; Phanerozoic Shale = 3.84 wt.% K_2O).

The CI-normalised rare earth element (REE) distributions of the three protolith samples are characterised by rectilinear and slightly fractionated patterns (La_N/Lu_N = 12–17; Fig. 12a) showing moderate negative Eu anomalies (Eu_N/Eu^* = 0.63–0.71). The pristine phyllite sample (MZ-1) has higher REE concentrations and also shows a slight negative Ce anomaly (Ce_N/Ce^* = 0.83).

The trace-element distribution of the quartzite sample S4 is very similar to that of the pristine phyllite MZ-1, with its much lower concentrations due to dilution by quartz (Figs 11a, 12a).

https://doi.org/10.1180/mgm.2022.42 Published online by Cambridge University Press

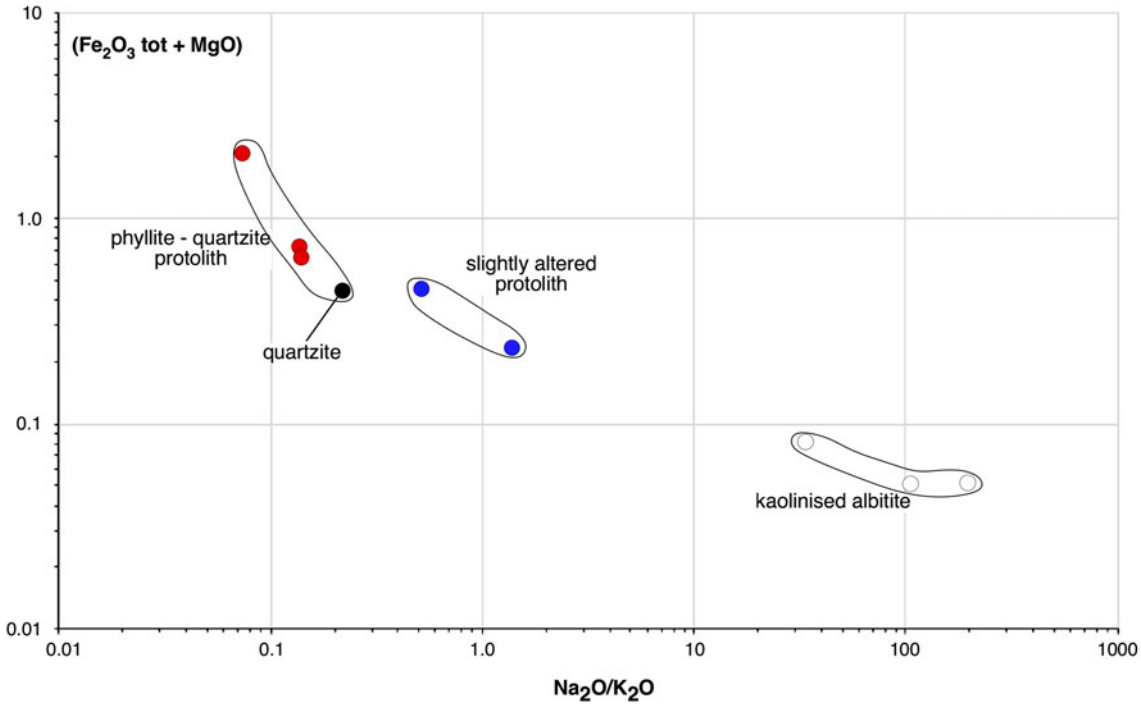

Fig. 10. (Fe_2O_3 tot + MgO) vs. Na_2O/K_2O (all in wt.%) diagram for the rocks studied.

The kaolinised albitite

The kaolinised albitite samples (S6, MZ-7 and MZ-17) are composed predominantly of SiO_2, Al_2O_3, Na_2O (Table 2). The Na_2O content is particularly high (3.2–5.9 wt.%) compared to those measured in the metasiliciclastic rocks of the Monte Serra Unit (generally Na_2O <1 wt.%; Franceschelli *et al.*, 1987). The high Na_2O is coupled with very low K_2O and, accordingly, the Na_2O/K_2O ratio is very high (34–200; Fig. 10). The TiO_2 contents are 1.0–1.3 wt.%, comparable to those measured in the phyllite rocks (1.0–1.1 wt.%).

The kaolinised albitite samples share similar trace-element distributions (Fig. 11b; Table 3) and differ from the pristine phyllite in their lower Li, Be, Sc, V, Ba, much lower Rb and Cs, and higher Sb (up to 278 µg/g) and Hg (up to 310 ng/g).

The CI-normalised REE patterns are generally rectilinear and slightly fractionated (La_N/Lu_N = 14–28; Fig. 12b) and show slightly negative Eu anomalies (Eu_N/Eu^* = 0.64–0.70). Overall, the REE abundances and relative distributions of the kaolinised albitite samples do not differ substantially from those of the pristine phyllite.

The Fe-hydroxide veins

The Fe-hydroxide veins are represented by sample MZ-9 which is composed mostly of Fe-hydroxide (Fe_2O_3tot = 65.8 wt.%, LOI = 18.0 wt.%), although it also contains a significant fraction of SiO_2, Al_2O_3, MnO and P_2O_5 (Table 2). The trace-element distribution of the sample is marked by a strong enrichment of Be, Sc, Cr, Co, Ni, Cu, Hg and U and a strong depletion in Rb, Cs, Nb, Ta and Th (Fig. 11b; Table 3). The high concentration of Hg (1650 ng/g) is particularly striking. In contrast, the concentration of Sb (27.3 µg/g) is comparable with that of the pristine phyllite. The CI-normalised REE pattern (Fig. 12b) shows an enrichment

Table 2. Major-element compositions (wt.%) of the rocks investigated.

Sample Rock type	S4 quartzite	MZ-1 phyllite	MZ-2 phyllite	St1d phyllite	MZ-15 intermediate	S5 intermediate	MZ-7 kaolinised albitite	MZ-17 kaolinised albitite	S6 kaolinised albitite	MZ-9 Fe-hydroxide vein
SiO_2	79.95	55.86	62.96	62.15	62.59	50.24	55.90	62.34	52.61	5.56
TiO_2	0.41	1.06	0.96	1.09	1.19	1.39	1.22	0.99	1.33	0.02
Al_2O_3	11.39	21.22	19.93	20.22	22.05	33.76	28.12	22.47	27.19	4.92
$Fe_2O_{3\ tot}$	2.12	8.23	4.79	5.22	2.51	1.00	0.97	1.13	4.06	65.81
MnO	0.08	0.07	0.06	<0.01	0.04	0.01	0.05	0.04	0.03	1.70
MgO	0.43	2.03	0.63	0.71	0.44	0.23	0.08	0.05	0.05	0.55
CaO	0.12	0.03	0.04	0.07	0.02	0.22	0.05	0.04	0.22	0.12
Na_2O	0.55	0.41	0.74	0.61	1.79	2.72	5.86	3.21	4.00	0.14
K_2O	2.47	5.55	5.15	4.37	3.36	1.97	0.17	0.03	0.02	<0.01
P_2O_5	0.02	0.05	0.03	0.09	0.09	0.06	0.08	0.09	0.22	1.56
LOI	2.14	4.09	3.67	4.03	6.00	9.35	7.87	10.11	8.93	17.96
Total	99.68	98.60	98.96	98.56	100.08	100.95	100.40	100.50	98.66	98.34
Na_2O/K_2O	0.22	0.07	0.14	0.14	0.53	1.38	34.5	107	200	-

LOI = loss on ignition

https://doi.org/10.1180/mgm.2022.42 Published online by Cambridge University Press

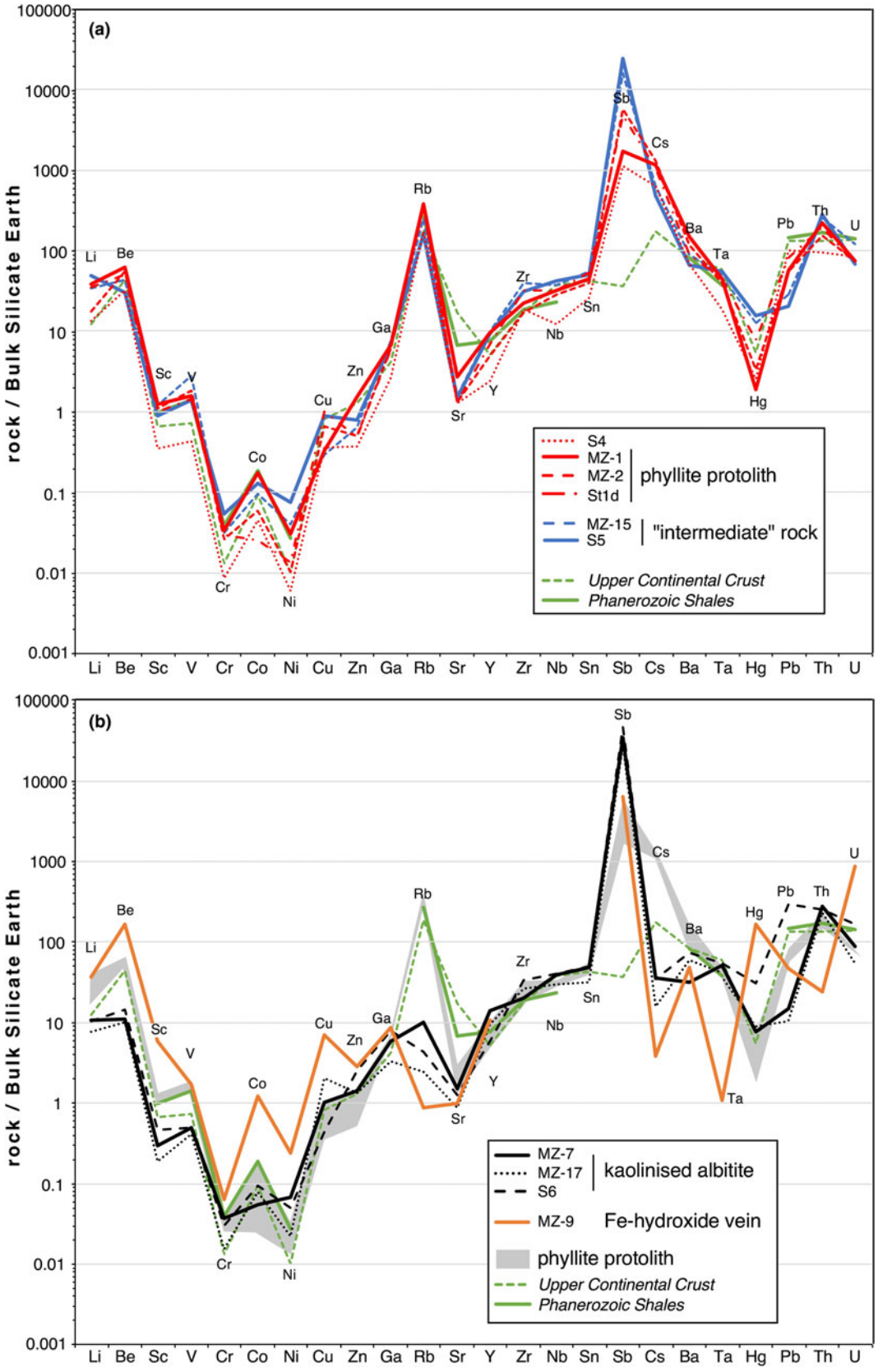

Fig. 11. Concentrations of trace elements in the samples investigated normalised to the Bulk Silicate Earth values (McDonough and Sun, 1995).

https://doi.org/10.1180/mgm.2022.42 Published online by Cambridge University Press

Table 3. Trace-element concentrations (μg/g) of the rocks studied.

	S4 quartzite	MZ-1 phyllite	MZ-2 phyllite	St1d phyllite	MZ-15 intermediate	S5 intermediate	MZ-7 kaolinised albitite	MZ-17 kaolinised albitite	S6 kaolinised albitite	MZ-9 Fe-hydroxide vein
Li	21.5	63	29.0	58	56	79	17.2	12.3	16.6	59
Be	2.19	4.3	3.8	3.5	3.03	2.12	0.76	0.69	0.98	11.2
Sc	5.7	20.2	18.3	16.6	19.6	14.7	4.8	3.1	7.5	94
V	36	130	151	121	233	115	41	34	40	141
Cr	23	88	69	79	83	142	98	41	78	169
Co	4.8	18.6	6.4	2.7	10.3	13.8	5.8	8.3	10.0	129
Ni	12.1	60	20.6	27	79	151	131	44	99	470
Cu	11	10	20	31	9	27	31	62	13	211
Zn	21	86	28	27	36	44	78	73	137	157
Ga	10.6	27.3	25.2	24.4	30.4	27.8	23.2	13.1	31.4	35
Rb	106	235	214	213	152	98	6.0	1.47	2.64	0.52
Sr	25.9	55	26.3	26.3	31.8	30.4	30.2	17.3	25.4	19.7
Y	10.4	42	21.6	30.5	43	41	60	41	25.4	46
Zr	197	242	183	342	421	331	211	280	350	<2
Nb	8.3	21.7	18.9	21.4	24.8	28.1	25.5	19.7	26.8	0.38
Sn	3.4	5.9	5.3	7.0	7.4	6.6	6.3	4.1	6.5	<0.1
Sb	6.2	9.6	32.3	26.5	89	135	188	151	257	35
Cs	13.4	24.4	27.6	22.9	13.6	10.3	0.74	0.33	0.73	0.08
Ba	457	1000	790	597	595	447	209	392	486	315
La	26.2	70	46	53	69	75	81	59	72	8.2
Ce	45	126	88	97	150	153	164	120	145	101
Pr	6.0	19.4	11.3	12.0	17.6	18.5	20.3	14.7	16.9	5.4
Nd	22.0	82	43	44	68	70	78	56	63	30.5
Sm	4.1	18.9	8.4	8.3	12.8	13.8	15.5	10.6	11.6	15.3
Eu	0.81	4.0	1.63	1.53	2.25	2.78	2.92	1.89	2.15	4.2
Gd	3.03	15.6	6.0	6.5	9.1	11.2	10.3	7.6	8.5	17.3
Tb	0.39	2.14	0.72	1.03	1.33	1.78	1.67	1.23	1.05	3.4
Dy	2.11	10.8	4.1	6.0	7.8	10.4	9.8	7.4	5.3	19.7
Ho	0.40	1.81	0.81	1.19	1.55	2.03	1.92	1.48	0.96	3.19
Er	1.11	4.7	2.35	3.5	4.5	5.7	5.4	4.1	2.63	8.9
Tm	0.16	0.63	0.33	0.51	0.64	0.77	0.77	0.55	0.35	1.43
Yb	0.96	3.8	2.03	3.09	3.9	4.4	4.5	3.06	1.94	10.0
Lu	0.13	0.57	0.28	0.44	0.54	0.61	0.62	0.42	0.27	1.30
Ta	0.70	1.66	1.47	1.68	1.90	2.05	1.92	1.52	2.00	0.04
Hg	0.026	0.019	0.034	0.080	0.115	0.157	0.076	0.088	0.309	1.65
Pb	15.5	8.7	8.4	12.4	4.4	3.08	2.23	1.60	44	7.1
Th	7.6	17.9	12.3	16.0	21.0	22.6	22.1	18.4	20.0	1.90
U	1.73	1.54	1.55	1.39	2.47	1.42	1.77	1.12	3.33	17.8

of the mid and heavy rare earth elements (MREE, HREE), a significant depletion of the light REE (LREE), a prominent positive Ce anomaly ($Ce_N/Ce^* = 3.7$), and a slight negative Eu anomaly ($Eu_N/Eu^* = 0.79$).

Fluid-inclusion data

Small (<0.5 mm) quartz crystals, grown during the Fe-carbonate ± quartz stage, were picked out from the breccia shown in Fig. 4f. These quartz crystals commonly host fluid inclusions, classified according to phase types occurring at room temperature. The inclusions were randomly distributed within quartz crystals and sometimes formed isolated clusters (Fig. 13a,b). They are assigned to a probable primary origin, according to the criteria of Roedder (1984). These inclusions are small in size (<20 μm, though most are <10 μm) and typically display an ellipsoidal morphology, though some examples have an irregular shape. Only one type of fluid inclusion was identified by microscopic observation at room temperature. These are two-phase (liquid + vapour) inclusions, liquid-rich at room temperature, having a vapour bubble that occupies ~20% of the inclusion volume. The results of microthermometric investigation are shown in Fig. 13c. During heating runs these inclusions homogenise by disappearance of the vapour bubble in the liquid phase at temperatures ranging between 159°C and 209°C with a mode at ~175°C. The small size of most of these inclusions does not allow the observation of initial ice melting during cryometric experiments (in only one case we observed initial ice melting at −52°C, suggesting the occurrence of divalent cations such as Ca^{2+}, Mg^{2+} and Fe^{2+}; Crawford, 1981). The final ice melting was observed in four fluid inclusions. The collected values consistently indicate a final ice melting temperature of ~−20.5°C, corresponding to salinity of ~23 wt.% NaCl equivalent, calculated according to Bodnar (1993).

Discussion

Mineralogical and textural evidence of hydrothermal reactions

The petrographic and mineralogical data have been used to reconstruct the mineral paragenetic sequence shown in Table 4. Different types of evidence have been used: (1) vein cross-cutting relationships; (2) mineral infilling sequences in veins; (3) mineral reaction textures (e.g. albite dissolution, Fe-hydroxide pseudomorphosis on Fe-carbonate); (4) changes in the relative proportions of mineral phases.

The first stage of the hydrothermal processes that affected the phyllite rocks is testified by the change in the proportions of albite vs. quartz and albite vs. 'potassic white mica' of the

https://doi.org/10.1180/mgm.2022.42 Published online by Cambridge University Press

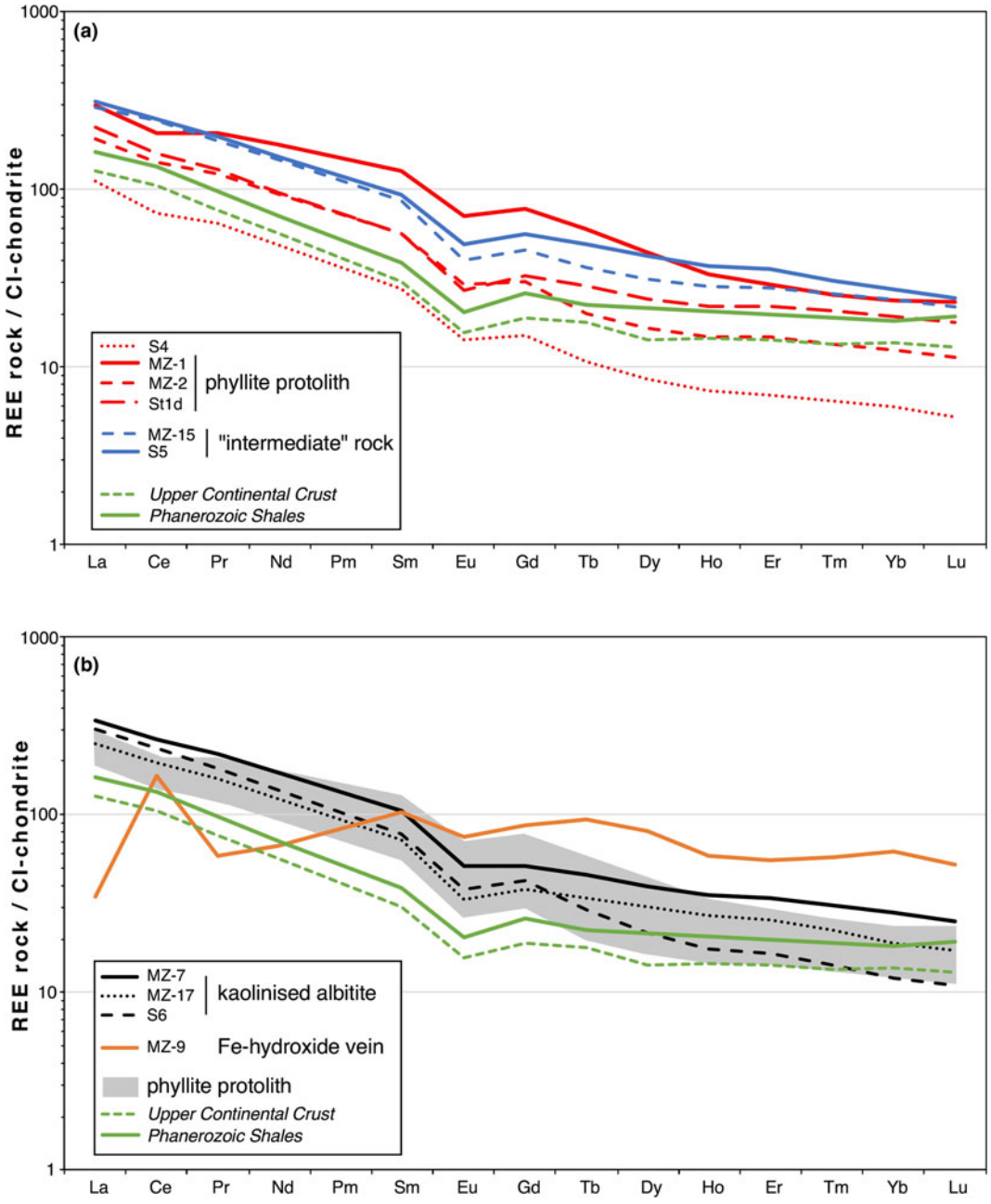

Fig. 12. Concentrations of the REE of the samples investigated normalised to the CI-chondrite values (McDonough and Sun, 1995).

kaolinised albitite compared to the protolith (Figs 5,6,7). This suggests quartz and 'potassic white mica' consumption and albite growth during the albitisation stage. A possible reaction, implying the involvement of a metasomatic fluid with extremely high Na/K ratio, and the removal of K^+, could be the following (Rosenbauer *et al.*, 1983):

$$\underset{\text{muscovite}}{KAlSi_3Al_2O_{10}(OH)_2} + \underset{\text{quartz}}{6SiO_2} + 3Na^+ = \underset{\text{albite}}{3NaAlSi_3O_8} + K^+ + 2H^+$$

Albitisation changes from 'replacement-type', generating diffuse granular albite, to 'vein-type', characterised by coarser albite crystals lining the walls of open fractures and vugs. Subsequently, the vein cross-cutting relationships and the mineral infill textures in veins (Fe-carbonate after albite) testify the Fe-carbonate ± quartz stage following albitisation (Figs 4, 9). The newly formed quartz is very scarce, however it is constantly found with Fe-carbonate, both in the veins and in the rock, indicating cessation of quartz dissolution reactions (Fig. 9e,f). The quartz crystals hosting two-phase L-rich fluid inclusions belong to this stage.

Subsequently, reaction features (partial dissolution of albite, Figs 7c,e, 9e; replacement of Fe-carbonate by Fe-hydroxides, Fig. 9) associated with the formation of kaolinite suggest a new hydrothermal stage (kaolinisation stage) induced by a pervasively

https://doi.org/10.1180/mgm.2022.42 Published online by Cambridge University Press

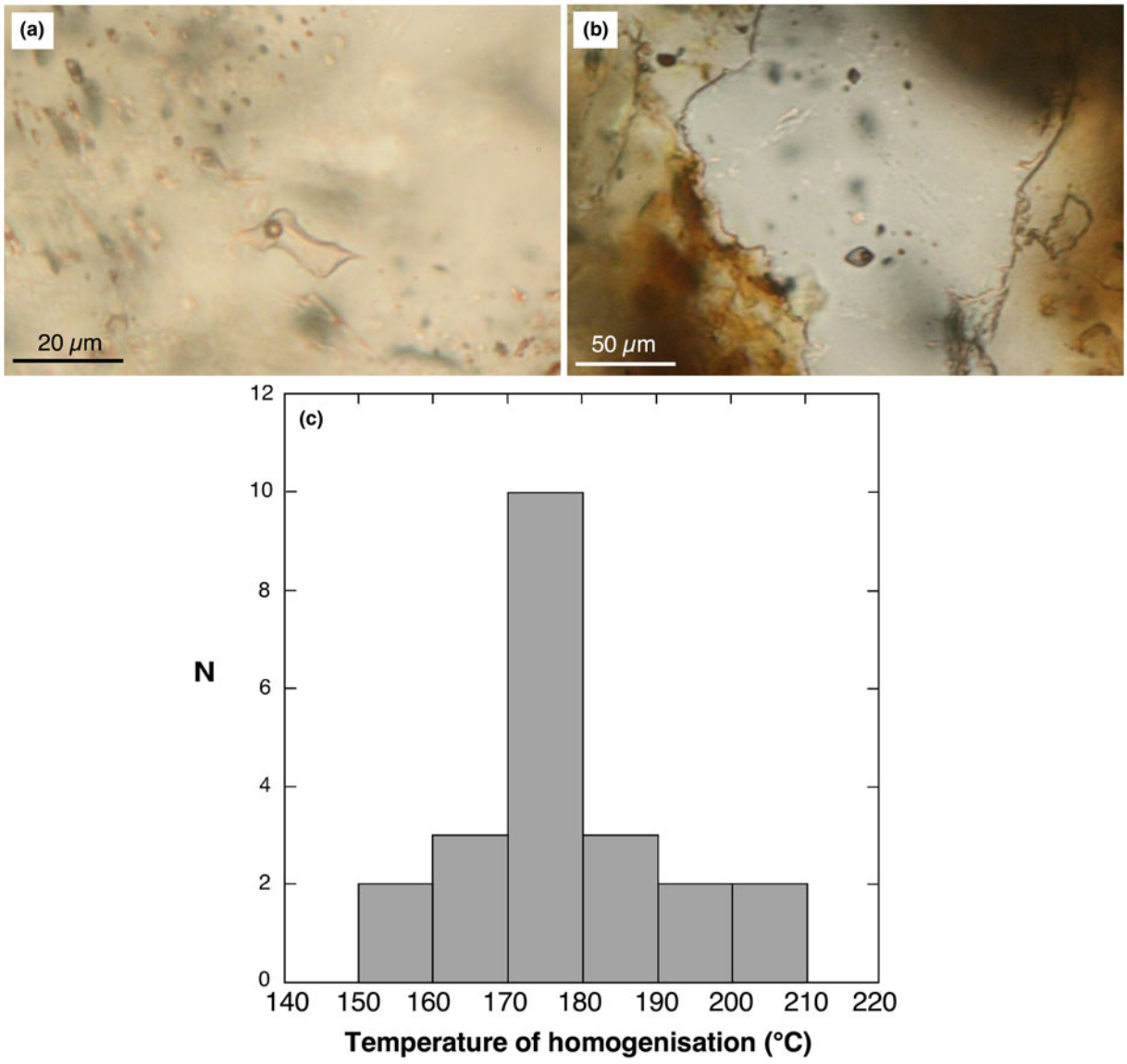

Fig. 13. Fluid inclusions in quartz: (a,b) photomicrographs of two-phase liquid-rich (L + V) primary fluid inclusions found within small quartz crystals in the brecciated kaolinised albitite; (c) histogram of the homogenisation temperatures (°C) of the studied fluid inclusions. *N* = number of measurements.

Table 4. Mineral paragenetic sequence for the alteration of the phyllite protolith.

	Albitisation stage	Fe-carbonate + quartz stage	Kaolinisation stage	Halloysite stage
Granular albite	----------			
Euhedral vein albite	--------			
Euhedral quartz		---		
Fe-carbonate		----------		
Kaolinite			----------	
Fe-hydroxide			----------	
(P–Al–Si)-bearing Fe-hydroxide				-----
Halloysite				----------

circulating, moderately acidic (pH ≈ 4–5) and oxidising fluid. A possible reaction could be the hydrolysis of albite (Blum, 1994):

$$2NaAlSi_3O_8 + 2H^+ + 9H_2O = Al_2Si_2O_5(OH)_4 + 4H_4SiO_4 + 2Na^+$$
albite → kaolinite

We suggest the euhedral albite lining veinlets and micro-vugs is preserved as the acidic fluid is neutralised by its reaction with Fe-carbonate.

Finally, the presence of halloysite as open space filling in veinlets (Figs 4e, 9a–d) and of several generations of Fe-hydroxides, in some cases sequestering P, Al and Si, lining cavities and veinlets, suggest the occurrence of late-stage supergene fluid circulation (halloysite stage).

https://doi.org/10.1180/mgm.2022.42 Published online by Cambridge University Press

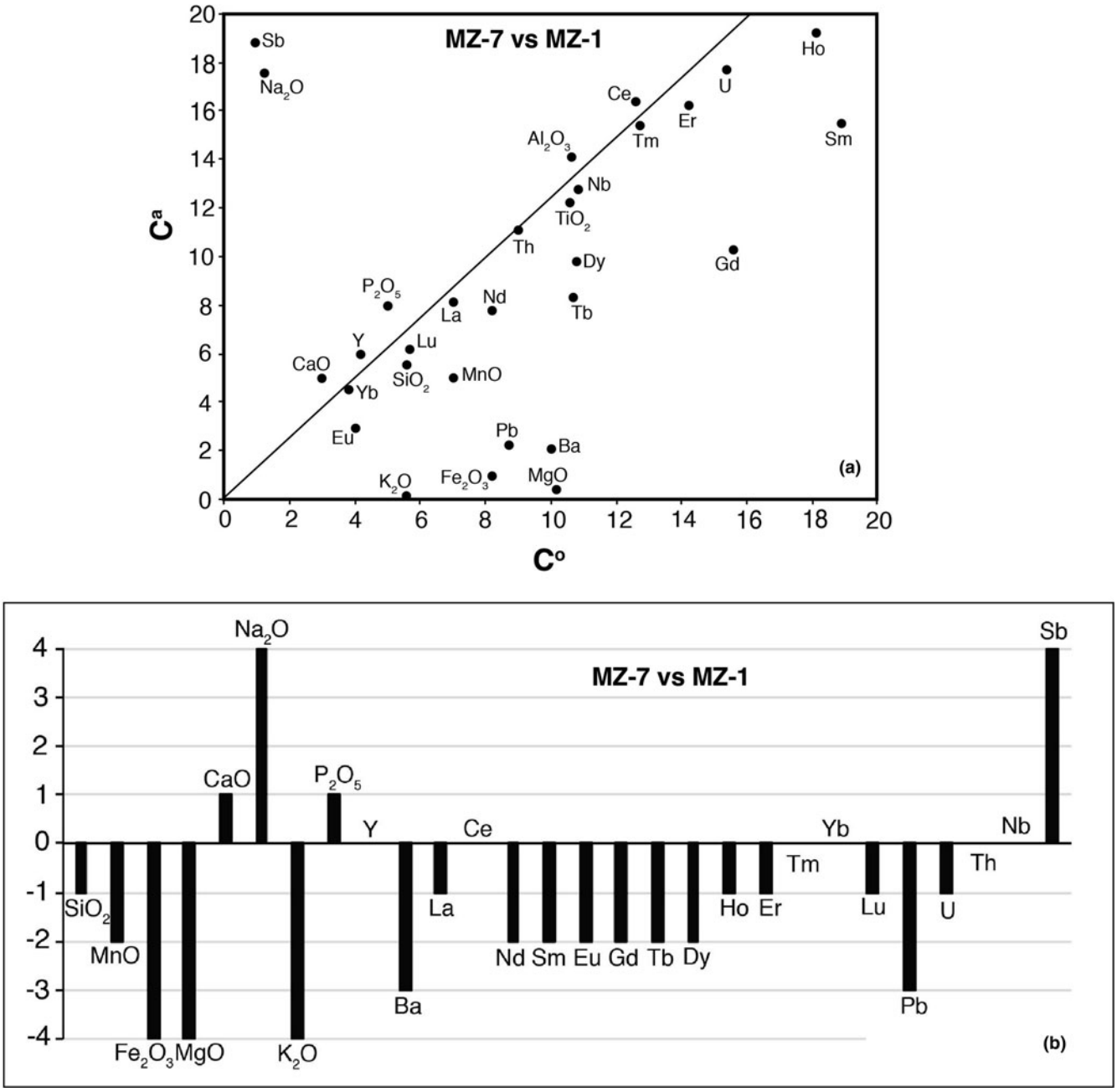

Fig. 14. Element mobility during the alteration processes: (a) isocon diagram for the kaolinised albitite sample MZ-7. Component abundances of fresh rock (sample MZ-1) are plotted on the horizontal scale, and those of its altered equivalent are plotted on the vertical scale; (b) histogram showing percentage of gains and losses of selected elements during alteration processes, as calculated from the isocon diagram presented in Fig. 14a. Variation of +4 to +1 = a gain of more than 100%, 50 to 100%, 25 to 50% and 10 to 25%, respectively. 0 = immobile elements (variation in the range + 10 and –10%). Values of –1 to –4 = losses of 10 to 25%, 25 to 50%, 50 to 90%, more than 90%, respectively.

Geochemical constraints on element mobility

The isocon method of Grant (1986) was employed for evaluating chemical gains and losses during the alteration processes. The altered rocks in this investigation consistently demonstrate the overlapping effects of the different alteration stages. As a consequence, it is not possible to quantify chemical gains and losses induced by any single alteration event; nonetheless, we tried to evaluate the elemental mobility in the course of the whole multistage hydrothermal alteration process, from the pristine phyllite to the final altered rocks. The isocon traced in this work was almost entirely controlled by the immobile elements Al and Ti, as commonly reported in several papers (i.e. Eaton and Setterfield, 1993; Mathieu, 2018; Pitzalis *et al.*, 2019). The isocon diagram is shown in Fig. 14a, and calculated (according to Grant, 1986) gains and losses for various elements due to hydrothermal alteration are plotted in Fig. 14b. These diagrams were built assuming the MZ-1 sample as fresh rock and MZ-7 sample as the most extreme kaolinised albitite. The results show a net gain of Na and Sb and a marked depletion of Fe, Mg, Mn, K, Ba and Pb. The overall effect

https://doi.org/10.1180/mgm.2022.42 Published online by Cambridge University Press

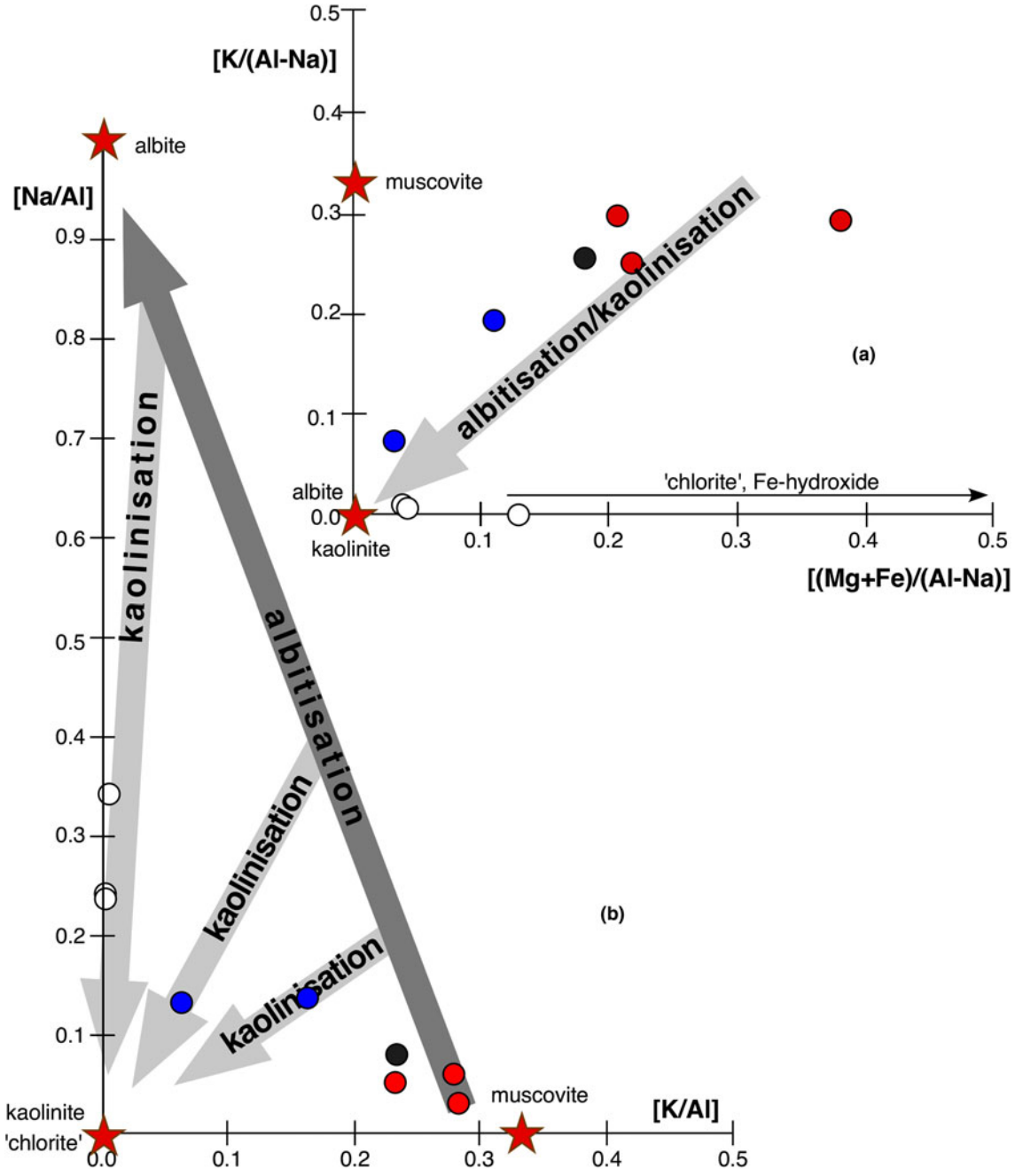

Fig. 15. Chemical model for the kaolinised albitite formation: (a) molar [K/(Al–Na)] vs. [(Mg+Fe)/(Al–Na)] for the rocks studied; (b) molar [Na/Al] vs. [K/Al] diagram for the rocks studied. Same symbols as in Fig. 10.

of the alteration process involves just a minor loss of Si. REE behaviour is characterised by depletion in the intermediate REE, whereas LREE and HREE are generally immobile.

Conclusions: evidence of a multi-stage hydrothermal process in the Monti Pisani area

This investigation documents the occurrence of localised multi-stage hydrothermal alteration of phyllite rocks from the Middle Triassic Verruca Formation. The process of albitisation undergone by the phyllite has not been observed before in the Monti Pisani area, and represents an interesting example of Na-metasomatism outside of a magmatic environment. The age of the hydrothermal processes is poorly constrained, however, due to the lack within the kaolinised albitite of the pervasive S_1 foliation observed in the pristine phyllite, it is very probably successive to the main deformative phase (D_1) of the Monti Pisani massif, which occurred during the Late Miocene (Rau and Tongiorgi, 1974). The high-Na/K metasomatic fluid induced a pervasive alteration of the pristine phyllite with loss of 'potassic white mica', quartz, 'chlorite' and hematite (Fig. 15a), and the conspicuous growth of hydrothermal albite. This stage induced a partial to nearly complete substitution of K by Na (Fig. 15b). The Na-rich fluids responsible for this alteration stage could be

https://doi.org/10.1180/mgm.2022.42 Published online by Cambridge University Press

originated from primary brines or from the interaction between hydrothermal fluids and evaporitic rocks (e.g. Quesnel *et al.*, 2019; Cathelineau *et al.*, 2021). These latter could be those originally hosted within the Triassic Calcare cavernoso Formation (Dini *et al.*, 1998; Montomoli *et al.*, 2005) or within the Scisti verdi member of the Quarziti di Monte Serra Formation. Indeed, Rau and Tongiorgi (1974) documented the occurrence of episodes of sedimentation inside hyperaline lagoons in the Scisti verdi succession.

The positive correlation between Na_2O and Sb observed in our samples suggests that Sb was carried by the Na-rich fluid. The occurrence of Sb-(Cr)-bearing Ti-oxide euhedral microcrystals in the kaolinised albitite indicates that the Sb introduced into the system during the albitisation stage was mainly fixed into this phase. As proposed by Smith and Perseil (1997) for the Sb-rich rutile from St. Marcel-Praborna Mn-mineralisation (Italy), and considering the systematic occurrence of Cr together with Sb in the rutile in the kaolinised albitite, the most probable cation exchange reaction could be:

$$2^{VI}Ti^{4+} = {}^{VI}[Al^{3+} + Cr^{3+} + Fe^{3+}] + {}^{VI}Sb^{5+}$$

The albitisation stage was followed by the formation of a system of Fe-carbonate ± quartz veins, which are a very common feature of the whole Monti Pisani area (Dini *et al.*, 1998). The fluid responsible for the formation of the Fe-carbonate ± quartz veins also pervaded the matrix of the albitite as testified by the occurrence of carbonate rhombohedra pseudomorphs (hosting euhedral quartz crystals; Fig. 9e,f). Fluid inclusions hosted in the quartz crystals indicate the circulation of high-salinity aqueous fluids (~23 wt.% NaCl equivalent) with a minimum temperature of ~175°C.

Fluids with greater salinity (33–41 wt.% NaCl equivalent) have been found in the Monti Pisani area by Dini *et al.* (1998) in hypersaline fluid inclusions (liquid + vapour + single halite crystal) hosted within quartz + Fe-carbonate (totally replaced by Fe-hydroxides) veins. These veins crop out 1.75 km due SW of the studied kaolinised albitite. On the basis of initial ice melting temperatures, the same authors hypothesised the occurrence of significant amounts of Ca^{2+}, Fe^{2+} and Mg^{2+} in addition to Na^+ and K^+ in these fluid inclusions. The subsequent alteration stage involved a slightly acidic and oxidising fluid, whose ingression was probably favoured by the increase of permeability accompanying albitisation, which led to the extensive replacement of albite by kaolinite and to the complete replacement of Fe-carbonate by Fe-hydroxides. The oxidising environment during this stage is also testified by the prominent positive Ce anomaly of the Fe-hydroxide veins (Fig. 12b; Bau, 1999). During this stage Na was partially removed from the rock (Fig. 15b). Successively, the ingression of supergene fluids led to the formation of widespread halloysite veinlets and colloform P–Al–Si-bearing Fe-hydroxides (last alteration minerals formed). The nearly immobile behaviour of LREE and HREE+Y could be due to the refractory nature of monazite-(Ce) and xenotime-(Y), respectively, during the different stages of the hydrothermal alteration process. The very last notable event undergone by these rocks was brittle deformation originating localised fracturing (Fig. 4f), without the formation of new minerals.

Prior to this work, the northernmost hydrothermally-altered rocks formed during the post-collisional phases of the Apennine Orogeny were found 30–40 km south of the Monte Zano area. Those occurrences are clearly related to the extensional tectonic setting which affected the Tyrrhenian side of Tuscany and involved lithospheric thinning and the emplacement of sialic and mafic magmas into the crust (Serri *et al.*, 1993). This geological framework led to the development of the intense and extensive hydrothermal activity that characterises central-southern Tuscany, where the Larderello and Mt Amiata high enthalpy active geothermal fields are the most striking and renowned occurrences (e.g. Batini *et al.*, 2003). Given this background, the kaolinised albitite in this investigation expands the effects of post-collisional hydrothermal activity in Tuscany northwards.

Acknowledgements. Funding of this study was provided by Pisa University's "Progetti di Ricerca di Ateneo - PRA–2020–25" granted to M. D'Orazio and A. Gioncada. The authors thank Ahmad Rabiee and an anonymous referee for their constructive reviews, and Roger Mitchell for the editorial handling. R. Ishak and M. Gemelli are acknowledged for their assistance at the FEG-SEM facility of the Centro per l'Integrazione della Strumentazione Scientifica dell'Università di Pisa (CISUP), P. Boulvais for the insightful comments on a previous version of the manuscript, C. Frassi for advice during field work, and C. Biagioni for the critical reading of the manuscript.

Competing interests. The authors declare none.

References

Barton M.D. and Johnson D.A. (1996) Evaporitic-source model for igneous-related Fe oxide-(REE-Cu-Au-U) mineralization. *Geology*, **24**, 259–262.

Batini F., Brogi A., Lazzarotto A., Liotta D. and Pandeli E. (2003) Geological features of Larderello-Travale and Mt. Amiata geothermal areas (southern Tuscany, Italy). *Episodes*, **26**, 239–244.

Bau M. (1999) Scavenging of dissolved yttrium and rare earths by precipitating iron oxyhydroxide: Experimental evidence for Ce oxidation, Y-Ho fractionation, and lanthanide tetrad effect. *Geochimica et Cosmochimica Acta*, **63**, 67–77.

Blum A.E. (1994) Feldspars in weathering. Pp. 595–630 in: *Feldspars and their reactions* (I. Parsons, editor). NATO ASI Series (Series C: Mathematical and Physical Sciences), vol. **421**. Springer, Dordrecht. https://doi.org/10.1007/978–94–011–1106–5_15.

Bodnar R.J. (1993) Revised equation and table for determining the freezing point depression of H_2O-NaCl solutions. *Geochimica et Cosmochimica Acta*, **57**, 683–684.

Boulvais P., Ruffet G., Cornichet J. and Mermet M. (2007) Cretaceous albitisation and dequartzification of Hercynian peraluminous granite in the Salvezines Massif (French Pyrénées). *Lithos*, **93**, 89–106.

Carten R.B. (1986) Sodium-calcium metasomatism: chemical, temporal, and spatial relationships at the Yerington, Nevada, porphyry copper deposit. *Economic Geology*, **81**, 1495–1519.

Castorina F., Masi U., Padalino G. and Palomba M. (2006) Constraints from geochemistry and Sr–Nd isotopes for the origin of albitite deposits from Central Sardinia (Italy). *Mineralium Deposita*, **41**, 323–338.

Cathelineau M. (1986) The hydrothermal alkali metasomatism effects on granitic rocks: quartz dissolution and related subsolidus changes. *Journal of Petrology*, **27**, 945–965.

Cathelineau M. (1987) U-Th-REE mobility during albitisation and quartz dissolution in granitoids: evidence from south-east French Massif Central. *Bulletin de Minéralogie*, **110**, 249–259.

Cathelineau M., Boiron M.-C. and Jakomulski H. (2021) Triassic evaporites: a vast reservoir of brines mobilized successively during rifting and thrusting in the Pyrenees. *Journal of the Geological Society*, **178**, 6.

Cavalcante F., Fiore S., Lettino A., Piccarreta G. and Tateo F. (2007) Illite-Smectite mixed layer in Sicilide shales and piggy-back deposits of the Gorgoglione Formation (Southern Apennines): geological inferences. *Bollettino della Società Geologica Italiana*, **126**, 241–254.

Cesarano M., Bish D.L., Cappelletti P., Cavalcante F., Belviso C. and Fiore S. (2018) Quantitative mineralogy of clay-rich siliciclastic landslide terrain of the Sorrento Peninsula, Italy, using a combined XRPD and XRF approach. *Clays and Clay Minerals*, **66**, 353–369.

Charoy B. and Pollard P.J. (1989) Albite-rich, silica-depleted metasomatic rocks at Emuford, Northeast Queensland; mineralogical, geochemical, and fluid inclusion constraints on hydrothermal evolution and tin mineralization. *Economic Geology*, **84**, 1850–1874.

https://doi.org/10.1180/mgm.2022.42 Published online by Cambridge University Press

Condie K.C. (1993) Chemical composition and evolution of the upper continental crust: contrasting results from surface samples and shales. *Chemical Geology*, **104**, 1–37.

Condit C.B., Mahan K.H., Curtis K.C. and Moller A. (2018) Dating metasomatism: Monazite and zircon growth during amphibolite facies albitisation. *Minerals*, **8**, 187, doi:10.3390/min8050187.

Crawford M.L. (1981) Phase equilibria in aqueous fluid inclusions. Pp. 75–100 in: *Short Course in Fluid Inclusions: Application to Petrology* (L.S. Hollister and M.L. Crawford, editors). Mineralogical Association of Canada, Vol. **6**.

Dini A., Orlandi P., Protano G. and Riccobono F. (1998) Le vene di quarzo del complesso metamorfico dei Monti Pisani (Toscana): caratterizzazione strutturale, mineralogia ed inclusioni fluide. *Atti della Società Toscana di Scienze Naturali, Memorie, Serie A*, **105**, 113–136.

Eaton P.C. and Setterfield T.N. (1993) The relationship between epithermal and porphyry hydrothermal systems within the Tavua Caldera, Fiji. *Economic Geology*, **88**, 1053–1083.

Engvik A.K., Putnis A., Fitz Gerald J.D. and Austrheim H. (2008) Albitisation of granitic rocks: The mechanism of replacement of oligoclase by albite. *The Canadian Mineralogist*, **46**, 1401–1415.

Franceschelli M., Leoni L., Memmi I. and Puxeddu M. (1986) Regional distribution of Al-silicates and metamorphic zonation in low-grade Verrucano metasediments from the Northern Apennines, Italy. *Journal of Metamorphic Geology*, **4**, 309–321.

Franceschelli M., Leoni L. and Sartori F. (1987) Geochemistry and mineralogy of detritic rocks from Verrucano type-sequences of Northern Apennines (Monti Pisani and Punta Bianca), Italy. *Rendicondi della Società Italiana di Mineralogia e Petrologia*, **42**, 13–31.

Franceschelli M., Leoni L. and Memmi I. (1989) b_0 of muscovite in low and high variance assembleges from low grade Verrucano rocks, Northern Apennines, Italy. *Schweizerische Mineralogische und Petrographische Mitteilungen*, **69**, 107–115.

Franceschelli M., Leoni L. and Sartori F. (1991) Crystallinity distribution and crystallinity-b0 relationships in white K-micas of Verrucano metasediments (Northern Apennins, Italy). *Schweizerische Mineralogische und Petrographische Mitteilungen*, **71**, 161–167.

Grant J.A. (1986) The isocon diagram—a simple solution to Gresens' equation for metasomatic alteration. *Economic Geology*, **81**, 1976–1982.

Holness M.B. (2003) Growth and albitisation of K-feldspar in crystalline rocks in the shallow crust: a tracer for fluid circulation during exhumation? *Geofluids*, **3**, 89–102.

Kaur P., Chaudhri N. and Eliyas N. (2019) Origin of trondhjemite and albitite at the expense of A-type granite, Aravalli orogen, India: Evidence from new metasomatic replacement fronts. *Geoscience Frontiers*, **10**, 1891–1913.

Kontonikas-Charos A., Ciobanu C.L. and Coo N.J. (2014) Albitisation and redistribution of REE and Y in IOCG systems: insights from Moonta-Wallaroo, Yorke Peninsula, South Australia. *Lithos*, 208–209, 178–201.

Krumm S. (1999) The Erlangen geological and mineralogical software collection. *Computers & Geosciences*, **25**, 489–499.

Leoni L., Lezzerini M. and Saitta M. (2008) Calcolo computerizzato dell'analisi mineralogica quantitativa di rocce e sedimenti argillosi basato sulla combinazione dei dati chimici e diffrattometrici. *Atti della Società Toscana di Scienze Naturali, Memorie, Serie A*, **113**, 63–69.

Leoni L., Montomoli C. and Carosi R. (2009) Il metamorfismo delle unità tettoniche dei Monti Pisani (Appennino Settentrionale). *Atti della Società Toscana di Scienze Naturali, Memorie, Serie A*, **114**, 61–73.

Mathieu L. (2018) Quantifying hydrothermal alteration: A review of methods. *Geosciences*, **8**, article number 245, doi:10.3390/geosciences8070245.

McDonough W.F. and Sun S.-S. (1995) Composition of the Earth. *Chemical Geology*, **120**, 223–253.

Montomoli C., Ruggieri G., Carosi R., Dini A. and Genovesi M. (2005) Fluid source and pressure-temperature conditions of high-salinity fluids in syntectonic veins from the Northeastern Apuan Alps (Northern Apennines, Italy). *Physics and Chemistry of the Earth*, **30**, 1005–1019.

Moore D.M. and Reynolds R.C. Jr (1997) *X-ray Diffraction and the Identification and Analysis of Clay Minerals*. Second edition. Oxford University Press, Oxford and New York, 400 pp.

Paoli G., Stokke H.H., Rocchi S., Sirevaag H., Ksienzyk A.K., Jacobs J. and Košler J. (2017) Basement provenance revealed by U–Pb detrital zircon ages: A tale of African and European heritage in Tuscany, Italy. *Lithos*, **277**, 376–387.

Pérez-Soba C. and Villaseca C. (2019) Li-Na-metasomatism related to I-type granite magmatism: A case study of the highly fractionated La Pedriza pluton (Iberian Variscan belt). *Lithos*, 344–345, 159–174.

Perez R.J. and Boles J.R. (2005) An empirically derived kinetic model for albitisation of detrital plagioclase. *American Journal of Science*, **305**, 312–343.

Petersson J., Stephens M.B., Mattsson H. and Möller C. (2012) Albitisation and quartz dissolution in Paleoproterozoic metagranites, central Sweden – Implications for the disposal of spent nuclear fuel in a deep geological repository. *Lithos*, **148**, 10–26.

Pirajno F. (2009) *Hydrothermal Processes and Mineral Systems*. Springer, 1250 pp.

Pitzalis E., Fulignati P., Lezzerini M., Cioni R., Pinarelli L., Tamponi M. and Gioncada A. (2019) Origin of volcanic-hosted Mn-oxide mineralization from San Pietro Island (SW Sardinia, Italy): An integrated geochemical, mineralogical and isotopic study. *Journal of Geochemical Exploration*, **204**, 206–223.

Quesnel B., Boiron M.-C., Cathelineau M., Truche L., Rigaudier T., Bardoux G., Agrinier P., de Saint Blanquat, M., Masini E. and Gaucher E.C. (2019) Nature and origin of mineralizing fluids in hyperextensional systems: the case of Cretaceous Mg metasomatism in the Pyrenees. *Geofluids*, **2019**, ID 7213050.

Rau A. and Tongiorgi M. (1974) Geologia dei Monti Pisani a sud-est della Valle del Guappero. *Memorie della Società Geologica Italiana*, **13**, 227–408.

Roedder E. (Editor) (1984) *Fluid Inclusions*. Reviews in Mineralogy, 12, Mineralogical Society of America, Washington, D.C., 646 pp.

Rosenbauer R.J., Bischoff J.L. and Radtke A.S. (1983) Hydrothermal alteration of graywacke and basalt by 4 molal NaCl. *Economic Geology*, **78**, 1701–1710.

Rubenach M.J. and Lewthwaite K.A. (2002) Metasomatic albitites and related biotite-rich schists from a low-pressure polymetamorphic terrane, Snake Creek Anticline, Mount Isa Inlier, north-eastern Australia: microstructures and P–T–d paths. *Journal of Metamorphic Geology*, **20**, 191–202.

Serri G., Innocenti F. and Manetti P. (1993) Geochemical and petrological evidence of the subduction of delaminated Adriatic continental lithosphere in the genesis of the Neogene-Quaternary magmatism of central Italy. *Tectonophysics*, **223**, 117–147.

Smith C. and Perseil E.-A. (1997) Sb -rich rutile in the manganese concentrations at St. Marcel-Praborna, Aosta Valley, Italy: petrology and crystal chemistry. *Mineralogical Magazine*, **61**, 655–669.

Taylor S.R. and McLennan S.M. (1995) The geochemical evolution of the continental crust. *Reviews in Geophysics*, **33**, 241–265.

Touret J. and Nijland T. (2013) Prograde, Peak and Retrograde Metamorphic Fluids and Associated Metasomatism in Upper Amphibolite to Granulite Facies Transition Zones. Pp. 415–469 in: *Metasomatism and the Chemical Transformation of Rock* (D.E. Harlov and H. Austrheim, editors). Springer, Berlin.

van de Kamp P. C. and Leake B. E. (1996) Petrology, geochemistry, and Na metasomatism of Triassic-Jurassic non-marine clastic sediments in the Newar, Hartford, and Deerfield rift basins, northeastern USA. *Chemical Geology*, **133**, 89–124.

https://doi.org/10.1180/mgm.2022.42 Published online by Cambridge University Press